*J. Fluid Mech.* (2007), *vol.* 585, *pp.* 1–40.  
doi:10.1017/S0022112007006076 Printed in the United Kingdom

# Pressure statistics and their scaling in high-Reynolds-number turbulent boundary layers

Y. TSUJI[1], J. H. M. FRANSSON[2], P. H. ALFREDSSON[2] AND A. V. JOHANSSON[2]

[1]Department of Energy Engineering and Science, Nagoya University, Nagoya 464-8603, Japan

[2]Linné Flow Centre, KTH Mechanics, SE-100 44 Stockholm, Sweden

(Received 7 June 2006 and in revised form 29 January 2007)

Pressure fluctuations are an important ingredient in turbulence, e.g. in the pressure strain terms which redistribute turbulence among the different fluctuating velocity components. The variation of the pressure fluctuations inside a turbulent boundary layer has hitherto been out of reach of experimental determination. The mechanisms of non-local pressure-related coupling between the different regions of the boundary layer have therefore remained poorly understood. One reason for this is the difficulty inherent in measuring the fluctuating pressure. We have developed a new technique to measure pressure fluctuations. In the present study, both mean and fluctuating pressure, wall pressure, and streamwise velocity have been measured simultaneously in turbulent boundary layers up to Reynolds numbers based on the momentum thickness $R_\theta \simeq 20\,000$. Results on mean and fluctuation distributions, spectra, Reynolds number dependence, and correlation functions are reported. Also, an attempt is made to test, for the first time, the existence of Kolmogorov's $-7/3$ power-law scaling of the pressure spectrum in the limit of high Reynolds numbers in a turbulent boundary layer.

## 1. Introduction

There is an immense body of literature on the behaviour, distribution and scaling of velocity fluctuations in turbulent boundary layers. However, so far very little is known about the corresponding behaviour of pressure fluctuations. The main reason for the lack of such results is that no measurement technique so far has been able to measure this quantity inside the boundary layer.

On the other hand wall pressure measurements beneath a turbulent boundary layer have been reported extensively. Extended reviews are given by Willmarth (1975), Eckelmann (1989), and Bull (1996), in which several unresolved issues and questions are summarized. One such point is the allowable ratio between the pressure transducer size and the smallest length scale in the flow. It is well known that insufficient resolution gives an attenuation of the spectrum in the high-frequency range. The effect of spatial averaging on the wall pressure was carefully studied by Schewe (1983) and correction methods have also been suggested (Corcos 1963). Recent progress has been made by the application of very small sensors based on MEMS (micro-electro-mecanical systems) technology. A survey of and outlook for microsensors can be found in Löfdahl & Gad-el-Hak (1999).

For incompressible flows, a Poisson equation for the pressure fluctuations is readily derived from the Navier–Stokes equation. The source term is composed of two parts with distinctly different character. One reflects the direct interaction between the gradient of the mean velocity field and the gradient of the turbulent fluctuating velocity field. The other part reflects turbulence–turbulence interaction. The two parts generate what is often referred to as the rapid and slow parts, respectively, of the pressure fluctuation field.

Early theoretical procedures relating a variety of pressure statistics to velocity and velocity derivative statistics were presented about fifty years ago. Heisenberg (1948), Obukhov (1949), Yaglom (1949), Batchelor (1951) and Inoue (1951) derived the spectral form and Reynolds number dependence of statistical moments under various assumptions. These results are summarized well in Monin & Yaglom (1971). The form of the pressure spectrum in the inertial range has in particular been the subject of many theoretical investigations. The direct parallel with the $-5/3$ Kolmogorov velocity fluctuation spectrum for the pressure field is a $-7/3$ region for the wavenumber dependence. However, in shear flows mean-shear interaction (and other factors) give other possibilities for the wavenumber dependence in this region.

Pioneering experiments to measure pressure fluctuations were performed by Kobashi (1957) and Kobashi, Kono & Nishi (1960), who measured the static pressure fluctuation behind the wake of a cylinder using a microphone. This technique was subsequently used by Toyoda, Okamoto & Shirahama (1993) for eduction of vortical structures in a non-circular jet, Iida *et al.* (1998) for detecting the aerodynamic sound source in the wake of a circular cylinder, and Naka *et al.* (2005) for evaluating the velocity–pressure correlation in a turbulent mixing layer. Jones *et al.* (1979) measured the one-dimensional power spectra of the turbulent static pressure fluctuations in the driven mixing layer of a subsonic circular jet. They also reported a simple dimensional analysis of the pressure spectrum in flows with mean shear. George, Beuther & Arndt (1984) developed a spectral model for turbulent pressure fluctuations and observed different types of power-law scaling forms for spectra from measurements in the mixing layer of an axisymmetric jet.

Pressure and velocity fluctuations were measured simultaneously by Elliot (1972) in an atmospheric boundary layer. He reported that the pressure spectra do not change with height above the surface, and found a power-law behaviour with a mean slope of $-1.7$ for high frequencies. A dominant feature of the pressure–velocity relationship is that the large-scale pressure fluctuations are approximately in phase with the streamwise velocity fluctuations. The effect of pressure forces on the energy flux from the streamwise velocity fluctuations was evaluated. This intercomponent redistributive energy flux was found to typically correspond to 0.45 of the streamwise turbulence production term (i.e. the transfer of energy from the mean flow to the streamwise fluctuating component). Albertson *et al.* (1998) also measured pressure fluctuations in the atmospheric surface layer over a grassy forest clearing and observed pressure spectra with a $-1.5$ power law.

Earlier experimental studies were focused on the shape of pressure spectra, but lacked information on the variation of pressure intensity across the boundary layer. Validation of experimentally obtained spectral data has been extremely difficult, but Tsuji & Ishihara (2003) were able to compare the experimental results with direct numerical simulation (DNS) data. They reported that the probability density function of pressure matched that of DNS well, and a power law close to $-7/3$ was realized in the range of Reynolds numbers based on the Taylor microscale ($\lambda$) and the intensity

of the streamwise velocity fluctutations ($u_{r.m.s.}$) $R_\lambda \geqslant 600$. These Reynolds numbers are about a factor of three higher than those needed for the velocity fluctuations to exhibit Kolmogorov scaling. They observed a spectral constant that is not universal but depends on Reynolds number.

This Reynolds number dependence is in accordance with the results of Gotoh & Rogallo (1999) who found that scaling of pressure and pressure gradient by Kolmogorov units appears inappropriate. A theoretical explanation of the Reynolds number dependence was given, which assumes that the small-scale pressure field is driven by coherent small-scale vorticity–strain domains. Similar results were obtained by Hill & Wilczak (1995) who derived a relationship between the pressure structure function and the fourth-order two-point correlation of velocity derivatives without using the joint Gaussian assumption. A modification of the spectral power-law exponent to account for the effect of turbulence intermittency was derived.

Direct numerical simulations have made a significant contribution to revealing the pressure characteristics in turbulence. For instance, Pumir (1994), Gotoh & Rogallo (1999), Vedula & Yeung (1999), Cao, Chen & Doolen (1999), Gotoh & Fukayama (2001), and Ishihara *et al.* (2003) have reported the statistical properties of pressure in a periodic box. For $R_\lambda \leqslant 732$ Ishihara *et al.* (2003) found that pressure has a power-law exponent different from that of the enstrophy and the energy dissipation rate. Alvelius & Johansson (2000) performed large-eddy simulation (LES) of forced anisotropic turbulence (at $R_\lambda = 516$) and identified a distinct $-7/3$ region in the pressure spectrum which was somewhat smaller than the corresponding $-5/3$ region for the velocity fluctuation spectrum. Pumir (1994) reported the pressure probability density function (PDF), which has an exponential tail on the negative side. Pumir observed this tail to be independent of Reynolds number for $R_\lambda \leqslant 60$. The joint PDFs of strain, vorticity, and pressure show a strong asymmetry between positive and negative pressure fluctuations.

Pressure fluctuations in a turbulent channel flow were investigated by Kim (1989), who examined probability density distributions, power spectra, and two-point correlations. When the pressure source term is divided into rapid (linear) and slow (nonlinear) parts, he found that the slow pressure fluctuations dominate throughout the channel except very near the wall. This result may appear somewhat unintuitive in view of the high values of non-dimensional shear rate in the near-wall region, but is a reflection of the non-local character of the pressure. Abe, Matsuo & Kawamura (2005) later confirmed the same trend in channel flow up to $Re_\tau = 1020$.

It has generally been found that the high-vorticity regions are strongly correlated with the low-pressure regions, implying that the pressure is one of the candidates to educe vortex structures (Kida & Miura 1998). Cadot, Douady & Couder (1995) characterized the low-pressure filaments by studying the correlations between the flow visualization and local measurement of pressure and velocity. The Lagrangian particle acceleration, $a_i \equiv \mathrm{D}u_i/\mathrm{D}t = -\rho^{-1}\partial p/\partial x_i + \nu\partial^2 u_i/\partial x_j \partial x_j$, can be approximated by the pressure derivative at sufficiently high Reynolds number. Voth, Satyanarayan & Bodenschatz (1998) and La Porta *et al.* (2001) reported acceleration measurements using a detector adapted from high-energy physics to track particles in a laboratory water flow. They found that the Kolmogorov scaling of acceleration variance is attained at high Reynolds numbers.

On the other hand Hill (2002) derived asymptotic formulae for fluid particle acceleration $a_i$, pressure gradient $-\rho^{-1}\partial p/\partial x_i$ and viscous force $\nu\partial^2 u_i/\partial x_j \partial x_j$. He concluded that fluid particle acceleration does not obey Kolmogorov scaling at any Reynolds number. Also Vedula & Yeung (1999) studied the scaling properties of

acceleration statistics using DNS data up to $R_\lambda = 230$ and concluded that Kolmogorov scaling was inappropriate.

The present study is the first attempt, as far as we know, to investigate the detailed pressure statistics in high-Reynolds-number turbulent boundary layers. Some of the results have been presented in Tsuji *et al.* (2005*a*). The accuracy of measured data is examined carefully and compared with DNS by Skote (2001), who computed the zero-pressure-gradient flow up to Reynolds numbers based on the momentum thickness ($\theta$) and the free-stream velocity $R_\theta = 716$. We believe that the present study reveals novel features of the pressure fluctuation field in high-Reynolds-number turbulent boundary layers.

The paper is organized as follows. The basic equations related to the pressure field are given in § 2 as well as a description of theoretical arguments for the scaling of the pressure spectrum. In § 3, the experimental conditions are detailed and the yaw angle effect, spatial resolution, resonance effect, and calibration methods are discussed in Appendix A. The experimental results are presented and discussed in § 4, and in the last section, we draw some final conclusions.

## 2. Theoretical considerations

### 2.1. *Basic equation for pressure fluctuation*

By taking the divergence of the Navier–Stokes equations, we obtain the Poisson equation for the instantaneous pressure $\tilde{p}$,

$$\frac{1}{\rho}\nabla^2\tilde{p} = -\frac{\partial \tilde{u}_i}{\partial x_j}\frac{\partial \tilde{u}_j}{\partial x_i}, \tag{2.1}$$

where $\tilde{u}_i$ is the instantaneous velocity for the $i$th-component. The Reynolds decomposition ($\tilde{p} = P + p$, $\tilde{u}_i = U_i + u_i$) of equation (2.1) leads to a Poisson equation for $p$ with two source terms:

$$\frac{1}{\rho}\nabla^2 p = -2\frac{\partial U_i}{\partial x_j}\frac{\partial u_j}{\partial x_i} - \frac{\partial^2}{\partial x_i \partial x_j}(u_i u_j - \langle u_i u_j \rangle), \tag{2.2}$$

where $\langle \ldots \rangle$ denotes the time average. On the basis of this equation, the fluctuating pressure field can be decomposed into three contributions:

$$p = p^{(r)} + p^{(s)} + p^{(h)}. \tag{2.3}$$

The rapid pressure $p^{(r)}$ satisfies

$$\frac{1}{\rho}\nabla^2 p^{(r)} = -2\frac{\partial U_i}{\partial x_j}\frac{\partial u_j}{\partial x_i}, \tag{2.4}$$

the slow pressure $p^{(s)}$ satisfies

$$\frac{1}{\rho}\nabla^2 p^{(s)} = -\frac{\partial^2}{\partial x_i \partial x_j}(u_i u_j - \langle u_i u_j \rangle), \tag{2.5}$$

and the harmonic pressure $p^{(h)}$ (sometimes referred to as the Stokes pressure) satisfies Laplace's equation $\nabla^2 p^{(h)} = 0$. The rapid pressure is so called because it responds immediately to a change in the mean velocity gradient and it dominates the slow part in the rapid-distortion limit. The harmonic (or Stokes) part can be shown to be negligible outside the immediate vicinity of the wall and is usually neglected. The second term in equation (2.2) can also be written as $(\partial u_i/\partial x_j)(\partial u_j/\partial x_i)$ which has

a strong form-similarity with the instantaneous dissipation-rate term. Accordingly, there is a close correspondence between strong low-pressure regions and intense thin vortical structures with high values of the dissipation rate (see e.g. Cadot *et al.* 1995).

### 2.2. *Spectral scaling of the pressure*

Kolmogorov presented hypotheses for small-scale statistics based on the idea of local isotropy (Monin & Yaglom 1971; Sreenivasan & Antonia 1997). For the form of the one-dimensional pressure spectrum $E_{pp}$ at high wavenumbers this implies,

$$E_{pp}(k_1) = \rho^2 \langle \varepsilon \rangle^{3/4} \nu^{7/4} \phi_p(k_1 \eta), \tag{2.6}$$

where $\phi_p$ is a non-dimensional function of the streamwise wavenumber ($k_1$) normalized by the Kolmogorov length scale $\eta$ defined as $\eta = (\nu^3/\langle \varepsilon \rangle)^{1/4}$, where $\langle \varepsilon \rangle$ is the energy dissipation rate per unit mass on average. Here, $\rho$ and $\nu$ denote the fluid density and the kinematic viscosity, respectively.

According to Kolmogorov's idea the spectrum exhibits an inertial subrange (for $k_1 \eta \ll 1$), when the Reynolds number becomes large, with a simpler form independent of $\nu$:

$$E_{pp}(k_1) = K_p \rho^2 \langle \varepsilon \rangle^{4/3} k_1^{-7/3}, \tag{2.7}$$

where $K_p$ is a universal constant.

The $-7/3$ power-law scaling was supported theoretically with various assumptions in the 1950s by Batchelor (1951), Inoue (1951), and Obukhov & Yaglom (1951). Recently, Tsuji & Ishihara (2003) have examined the pressure spectrum in fully developed nearly isotropic turbulence in the centre of a plane jet for the Reynolds number range of $200 \leqslant R_\lambda \leqslant 1200$. A power-law exponent of the pressure spectrum was systematically obtained by fitting the relation

$$E_{pp}(k_1) = K'_p \rho^2 \langle \varepsilon \rangle^{3/4} \nu^{7/4} (k_1 \eta)^{\gamma_p} \tag{2.8}$$

to the measured spectrum, where $K'_p$ is a non-dimensional quantity. The value of $\gamma_p$ that gave the broadest flat region for the normalized spectrum $E_{pp}/(k_1\eta)^{\gamma_p}$ was determined for each case. They concluded that if the scaling exponent $\gamma_p$ is plotted as a function of $R_\lambda$, it indeed departs from $-7/3$ at low Reynolds numbers, but that the exponent approaches $-7/3$ as the Reynolds number is increased. The $-7/3$ power-law scaling was confirmed for $R_\lambda \geqslant 600$. This is a significantly higher Reynolds number than needed for inertial-range scaling of velocity statistics. The pressure spectrum has a noticeably narrower scaling region than the velocity, which is consistent with the result that a higher Reynolds number is needed to realize a clear $-7/3$ power-law scaling.

Not only the Reynolds number but also the shear effect is indispensable in considering the power-law exponent. In this paper we examine the Kolmogorov scaling of pressure in the turbulent boundary layer, and evaluate the effects of both shear and Reynolds number in making $\gamma_p$ deviate from $-7/3$. The spectral slope, for $\gamma_p$ determination, is carefully computed in §4.2.3 and the procedure is outlined in Appendix B.

### 2.3. *Other models for spectral scaling*

A scaling law for the velocity spectra was suggested by Townsend (1976) and was further developed by Perry, Henbest & Chong (1986). The argument is based on Townsend's *attached eddy hypothesis*, which assumed that a turbulent boundary layer may be modelled as a forest of hairpin or $\Lambda$-shaped vortices. All eddies are not only geometrically similar but have the same dependence on the distance from the wall.

Using this idea in conjunction with dimensional analysis, scaling laws for the energy spectra were derived.

Bradshaw (1967*a*) discussed the wall pressure spectra using this concept of attached eddies. He divided the region $y/\delta < 0.2$ ($y$ being the wall-normal coordinate and $\delta$ the boundary layer thickness) into two essentially independent parts: a high-intensity vorticity-dominated inner layer and a region with large-scale inactive motion in the outer layer. Assuming that the former part is universal with the friction velocity scale $u_\tau$ $(=(\tau_w/\rho)^{1/2}$, where $\tau_w$ is the wall shear stress) and the length scale $y$, a spectral form, $E_{pp} \sim k_1^{-1}$, was suggested. Further theoretical discussions are in Panton & Linebarger (1974).

The concept of the attached eddy hypothesis might be useful not only for the wall pressure but also for the static pressure in the boundary layer. Here, the pressure spectra are studied from the viewpoint of Perry's scaling. Pressure is a non-local quantity and it may be difficult to connect its origin to the $\Lambda$-shaped vortices, but we have found some positive correlation between streamwise velocity and pressure fluctuation, which will be mentioned in the result section, and thus a similar dimensional analysis may be convenient to use for investigation of the spectral features of pressure.

For the large-scale eddies, viscosity has negligible influence and the spectrum in the low-wavenumber region should only depend on $u_\tau$, $k_1$, $y$, and $\delta$. For our analysis of experimental data the streamwise wavenumber is defined as $k_1 \equiv 2\pi f/U$, where $f$ is the frequency and $U$ the local mean velocity. A dimensional analysis gives the spectrum of $p$ at low wavenumbers as

$$\frac{E_{pp}(k_1)}{\rho^2 u_\tau^4 \delta} = g_1(k_1\delta). \tag{2.9}$$

This is an 'outer-flow' scaling and it mainly describes the effects of large-scale eddies. On the other hand, eddies of scale $y$ will contribute to the intermediate-wavenumber range (where viscosity still is of negligible influence) of the spectrum. Thus the spectrum in this range should follow the scaling form

$$\frac{E_{pp}(k_1)}{\rho^2 u_\tau^4 y} = g_2(k_1 y). \tag{2.10}$$

It is expected that equations (2.9) and (2.10) will have a region of overlap (overlap region I). From the dimensional requirement, in overlap region I, the spectra should have the form $g_2(k_1y)/g_1(k_1\delta) = \delta/y$. Then one possible functional form is given by Perry *et al.* (1986) as

$$g_1(k_1\delta) = \frac{A_1}{k_1\delta}, \quad g_2(k_1 y) = \frac{A_1}{k_1 y}, \tag{2.11}$$

where $A_1$ is thought to be a universal constant. Thus the $-1$ power-law region can be expected to be observed in the low-wavenumber range.

The small-scale motions, which contribute to the high-wavenumber range of the spectrum, may be expected to follow the Kolmogorov scaling. Kolmogorov assumed that these small-scale motions are locally isotropic, and that their energy content will depend only on the local rate of turbulence energy dissipation and the kinematic viscosity. Dimensional analysis leads to the spectral form

$$\frac{E_{pp}(k_1)}{\rho^2 \upsilon^4 \eta} = g_3(k_1\eta), \tag{2.12}$$

| Case | $U_0$ [m s$^{-1}$] | $u_\tau$ [m s$^{-1}$] | $\Delta$ [m] | $\delta$ [mm] | $\delta^*$ [mm] | $\theta$ [mm] | $R_\theta$ |
|---|---|---|---|---|---|---|---|
| 1 | 8.3 | 0.33 | 0.36 | 62.9 | 13.2 | 10.3 | 5870 |
| 2 | 11.5 | 0.43 | 0.34 | 59.8 | 12.6 | 9.4 | 7420 |
| 3 | 14.6 | 0.53 | 0.33 | 57.8 | 12.2 | 8.9 | 8920 |
| 4 | 17.9 | 0.63 | 0.33 | 56.5 | 11.8 | 8.6 | 10500 |
| 5 | 21.2 | 0.74 | 0.32 | 55.4 | 11.5 | 8.3 | 12100 |
| 6 | 24.4 | 0.84 | 0.32 | 55.3 | 11.2 | 8.2 | 13600 |
| 7 | 27.7 | 0.94 | 0.32 | 54.1 | 11.0 | 8.0 | 15200 |
| 8 | 30.8 | 1.04 | 0.31 | 53.6 | 10.7 | 7.9 | 16700 |
| 9 | 34.0 | 1.14 | 0.31 | 53.2 | 10.5 | 7.8 | 18300 |

TABLE 1. Characteristics of the boundary layer. The experiments are performed several times for each condition. $U_0$ is the free-stream velocity and $u_\tau$ is the friction velocity. $\delta$ is the boundary layer thickness taken at $U(\delta) = 0.95U_0$, $\theta$ is the momentum thickness, and $\delta^*$ is the displacement thickness. $\Delta$ is the Rotta–Clauser boundary layer thickness defined as $\Delta \equiv \int_0^\infty (U_0 - U(y))/u_\tau \mathrm{d}y$.

where $\upsilon$ is the Kolmogorov velocity scale defined as $\upsilon = (\nu\langle\varepsilon\rangle)^{1/4}$. It is expected that equations (2.10) and (2.12) will have a region of overlap (overlap region II). In overlap region II, referred to as the inertial subrange, the spectrum follows the Kolmogorov scaling,

$$g_3(k_1\eta) = \frac{K_p}{(k_1\eta)^{7/3}}, \tag{2.13}$$

where $K_p$ is expected to be a universal constant (cf. equation (2.7)). In the spectral overlap region II, (2.10) matches (2.13), where the form of the spectrum is given by

$$\frac{E_{pp}(k_1)}{\rho^2 u_\tau^4 y} = \frac{B_1}{(k_1 y)^{7/3}}. \tag{2.14}$$

This spectral form is derived from the assumption that the distance from the wall represents a position in the log-region (the physical overlap region), where the energy dissipation rate can be evaluated by the relation $\langle\varepsilon\rangle = -\langle uv\rangle \mathrm{d}U/\mathrm{d}y$, and $-\langle uv\rangle = u_\tau^2$. In the log-region $\mathrm{d}U^+/\mathrm{d}y^+ = A/y^+$. The constant $B_1$ is hence equal to $K_p A^{4/3}$.

## 3. Experimental conditions

The experiments were performed in the MTL (Minimum Turbulence Level) wind tunnel at KTH. This is a high-quality flow tunnel with a streamwise turbulence intensity of less than 0.025 % and a total pressure variation less than $\pm 0.06$ % across the test section at a free-stream velocity of 25 m s$^{-1}$ (see Lindgren 2002, for further details about the MTL wind tunnel). The present experimental conditions are matched with those of Österlund (1999) which cover the Reynolds number range $2600 \leqslant R_\theta \leqslant 26\,700$. In the present work we have utilized nine different Reynolds numbers in the range $5870 \leqslant R_\theta \leqslant 18\,300$ where the measurement station is 5.5 m from the leading edge, and the boundary layer characteristics for the various cases are summarized in table 1. Details of the experimental setup are not repeated here, but given in Österlund (1999).

### 3.1. *Boundary layer pressure measurements*

The measurement of pressure fluctuations in the flow field is accomplished with standard static pressure tube probes of different dimensions and with two different sensors. See figure 1 for a sketch of the probe. In this experiment five different probe

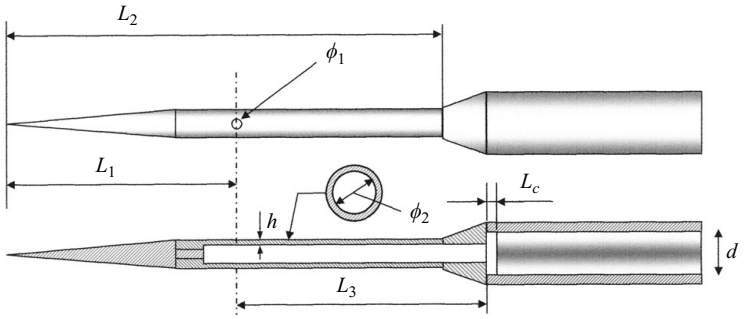


FIGURE 1. Schematic view of the static pressure probe.

| | Symbols in figures 24–26 | $\phi_1$ | $\phi_2$ | $L_1$ | $L_2$ | $L_3$ |
|---|---|---|---|---|---|---|
| probe 1 | △ | 0.20 | 1.0 | 22.5 | 47.5 | 30.0 |
| probe 2 | ○ | 0.15 | 0.5 | 15.5 | 27.5 | 16.0 |
| probe 3 | ▽ | 0.20 | 0.7 | 15.5 | 27.5 | 18.5 |
| probe 4 | □ | 0.40 | 1.0 | 22.5 | 47.5 | 30.0 |
| probe 5 | ◇ | 0.30 | 1.0 | 22.5 | 47.5 | 30.0 |

TABLE 2. Static pressure probe dimensions used in the present experiments (see figure 1 for a sketch of the probe).

configurations are used, which are listed in table 2. This type of pressure probe has previously been used by Kobashi (1957) and Toyoda *et al.* (1993); however, in the present study the probe is much smaller than in the previous measurements (cf. Tsuji & Ishihara 2003).

The probe body consists of two stainless steel tubes joined by threaded and screwed junctions, with the windward tube cone-shaped and equipped with four static pinholes spaced 90° in the circumferential direction and located a distance $L_1$ from the tip. This tube has pinhole diameters of $\phi_1$ mm, inner diameters of $\phi_2$ mm, and a material tube thickness of $h = 0.05$ mm.

The leeward tube has at its end one of the two sensors, which are a small piezoresistive transducer and a standard quarter-inch condenser microphone with diameters $d_T = 1.6$ mm and $d_M = 7.0$ mm, respectively. The transducer has a frequency response from DC up to 150 kHz with a dynamic range of $0 \sim 3.5 \times 10^3$ Pa, and the maximum errors in linearity and hysteresis are 0.25 % of the measured value. The microphone can measure in the frequency range $10 \sim 70 \times 10^3$ Hz, where the lower frequency limit is determined by its mechanical system. The dynamical range is $2 \times 10^{-4} \sim 3.2 \times 10^3$ Pa, implying that relatively small amplitudes can be measured.

A schematic view of the experimental set-up is shown in figure 2. Here, a specially designed wall-normal traversing system is used, which protrudes from the plate and allows traversing in the range $0 \leqslant y \leqslant 120$ mm. Simultaneously with the static pressure measurements the streamwise velocity component is acquired by means of a single hot wire anemometer operated in constant-temperature mode. The hot wire is positioned vertically and about 1.0 mm adjacent to the static pressure probe pinholes. In the present context, static pressure fluctuation is sometimes referred to simply as pressure fluctuation, and it is denoted $p_s$.

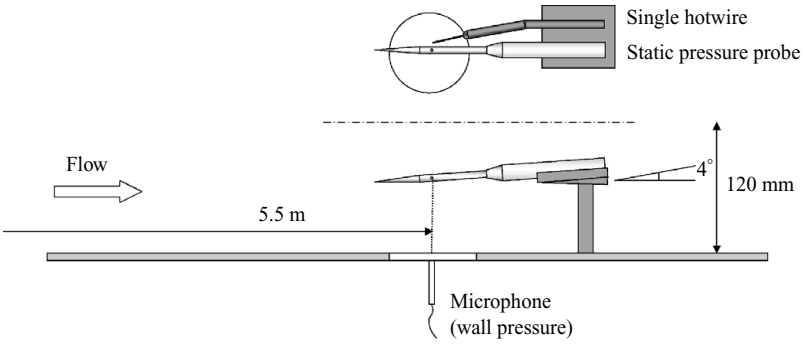


FIGURE 2. Schematic view of the experimental set-up.

### 3.2. *Wall pressure measurements*

The pressure at the wall can be measured by various configurations and most involve a pinhole in the boundary surface with a piezoelectric transducer or a microphone mounted below. Bull (1996) classified different measurement configurations as follows:

(1) A condenser microphone mounted in a cavity behind the surface pinhole.
(2) A piezo-electric transducer mounted behind the pinhole.
(3) A piezo-electric transducer mounted behind the pinhole without a cavity.
(4) A piezo-electric transducer mounted behind the pinhole without a cavity, but with the pinhole filled with silicone grease to restore a continuous boundary surface.
(5) A piezo-electric transducer mounted flush with the boundary surface with no surface discontinuity.

For mean pressure measurements at the wall, previous experiments have shown that the pressure recorded through a pinhole is normally somewhat higher than the 'true' value. The pressure error, $\Delta p_w \equiv$ (measured value)$-$(true value), depends on the pinhole diameter $d$, the hole depth $\ell$, the diameter of the connection to the sensor $d_c$, the wall shear stress $\tau_w$ $(= \rho u_\tau^2)$, the kinematic viscosity $\nu$, and the characteristic length scale of the facility $D$. Thus, the non-dimensional pressure error for a finite hole size can be written as (Shaw 1960)

$$\frac{\Delta p_w}{\tau_w} = f\left(\frac{du_\tau}{\nu}, \frac{d}{D}, \frac{\ell}{d}, \frac{d_c}{d}\right). \tag{3.1}$$

Shaw noted that the non-dimensional pressure error is always positive but approaches zero with decreasing $d$, increases with increasing $d^+ = du_\tau/\nu$ but reaches an asymptotic limit, and increases with $\ell/d$ but asymptotes to a constant value when $\ell/d$ approaches $1.5 \sim 2$.

The influence of pinholes, in flat-plate boundary layers, in measuring wall pressure fluctuations has been reported by several investigators and with varied enthusiasm. Bull (1996) concluded that pinholes are responsible for local flow disturbances leading to errors in the measured data, while Farabee & Casarella (1986, 1991) and Gedney & Leehey (1991) concluded that pinhole sensors are indeed effective for wall-pressure measurements.

That the effect of the sensor's spatial resolution is of primary importance was pointed out by Keith, Hurdis & Abraham (1992). This was later supported by Gravante *et al.* (1998) who reported that the allowable non-dimensional sensing diameter to avoid spectral attenuation for frequencies up to $f^+ = f\nu/u_\tau^2 = 1$ is in the

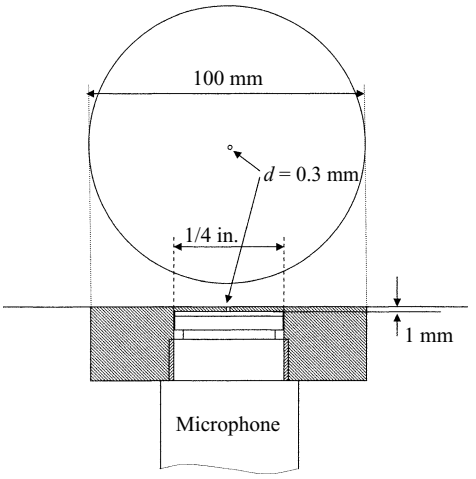


FIGURE 3. Schematic view of pinhole arrangement for wall pressure measurements.

range of $12 \leqslant d^+ \leqslant 18$. They compared the wall-pressure spectrum with that by Schewe (1983) and the agreement was excellent. Since Schewe did not use a pinhole but instead used the Sell type transducer technique, the coincidence of their spectra proves that the pinhole is effective for wall-pressure measurements if reasonably small pinhole sizes are used. Lueptow (1995) evaluated the pinhole size to be less than 20 viscous wall units for an insignificant spectral attenuation.

On the use of pinholes for wall pressure measurements, in summary the following criteria are required. (i) pinhole size should be small enough compared with the length scale in the flow, that is $d^+ < 20$; (ii) the aspect ratio $\ell/d$ should satisfy the condition $\ell/d \geqslant 2$; (iii) the effect of Helmholtz resonance should be removed or the resonance frequency peak set in the high-frequency range; (iv) background noise correction is necessary especially for low Reynolds number flow. In the present experiment, wall-pressure fluctuations are measured by methods (1), (2), and (3) listed above. As shown in figure 3 the 1/4 inch microphone is mounted in the cavity volume behind the surface, which is arranged to be as small as possible. The pinhole diameter is $d = 0.3$ mm and its depth is $\ell = 1.0$ mm. Hence the normalized pinhole diameter is in the range $4.6 \leqslant d^+ \leqslant 20.7$ depending on Reynolds number, and the aspect ratio is $\ell/d = 3.33$. Thus the error is estimated to be minimal. In this context, the wall pressure fluctuation is denoted $p_w$.

### 3.3. *Calibration of static pressure probe*

In this subsection we briefly summarize the main results from the static pressure probe calibration. A detailed description of the calibration is given in Appendix A.

In order to achieve accurate measurements, both the mean and fluctuations of the measured pressure signal are corrected according to the appropriate calibration. For the mean pressure, the effect of pinhole size and tube thickness is corrected. The amplitude ratio and phase delay in instantaneous pressure caused by the Helmholtz-resonator is removed numerically from the measured signal. The present probe has the following performance. Yaw angle effect is shown to be negligible in the range of $-5^\circ \leqslant \theta \leqslant 5^\circ$. The standing wave generated inside the tube restricts the time frequency response to below 10 kHz. The spatial resolution is around the Kolmogorov length scale. Finally, the correction of background noise in the statistical sense can be assumed to be negligible in the inner region. In the course of this experiment we used

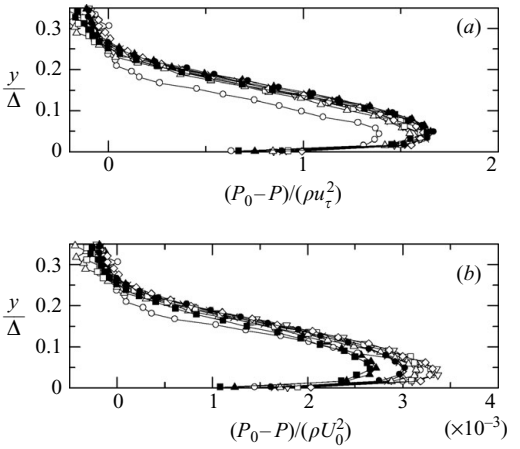


FIGURE 4. (*a*) Mean pressure profile in the boundary layer in absolute terms. $P_0$ is the wall pressure. Distance from the wall $y$ is normalized by the Rotta–Clauser thickness. (*b*) Same data but normalized with twice the dynamic pressure. Symbols indicate the different Reynolds numbers. ○, $R_\theta = 5870$; △, $R_\theta = 7420$; □, $R_\theta = 8920$; ▽, $R_\theta = 10\,500$; ◇, $R_\theta = 12\,100$; ×, $R_\theta = 13\,600$; ●, $R_\theta = 15\,200$; ▲, $R_\theta = 16\,700$; ■, $R_\theta = 18\,300$.

probe2 and probe3 (see table 2). For the wall pressure measurement, if there is a cavity behind the surface pinhole, Helmholtz resonance is generated. Then the same numerical correction is applied.

## 4. Results and discussion

### 4.1. *Mean pressure profile*

Mean pressure distributions are plotted in figure 4 for the nine different Reynolds numbers listed in table 1. The distance from the wall, $y$, is normalized by the Rotta–Clauser boundary layer thickness $\Delta$ (see the caption of table 1), and the pressure throughout the boundary layer $P(y)$ is subtracted from a reference pressure $P_0$. This reference pressure was chosen to be the wall pressure since its position is well defined, the access is continuous, and it gave the most consistent results. Under ideal conditions the free-stream pressure should match the wall pressure, but as indicated in figure 4 the wall pressure is slightly lower than the free-stream pressure. It should be noted that the pressure differences are small, but when normalizing the different Reynolds number data with their respective free-stream dynamic pressure the distributions all collapse fairly well on top of each other, strengthening our confidence in the measurements. Note that the mean pressure is affected by the wall up to $y \simeq 0.3\Delta$ and that the peak of $\Delta P_M = P_0 - P$ is located around $y \simeq 0.05\Delta$ (although there is a tendency for the peak to move slightly away from the wall with increasing Reynolds number). The boundary layer thickness, $\delta$, can roughly be estimated as $\Delta/6$.

The turbulent boundary layer momentum equation normal to the plate shows that the mean static pressure $P(y)$ varies with the distance from the wall as

$$P(y)/\rho \approx P_0^*/\rho - \langle v^2 \rangle, \tag{4.1}$$

if the streamwise Reynolds stress gradient is neglected compared to the cross-stream gradient terms. Upon integration with respect to the wall-normal direction to obtain (4.1) it can easily be shown that the Reynolds stress term is a few orders of magnitude

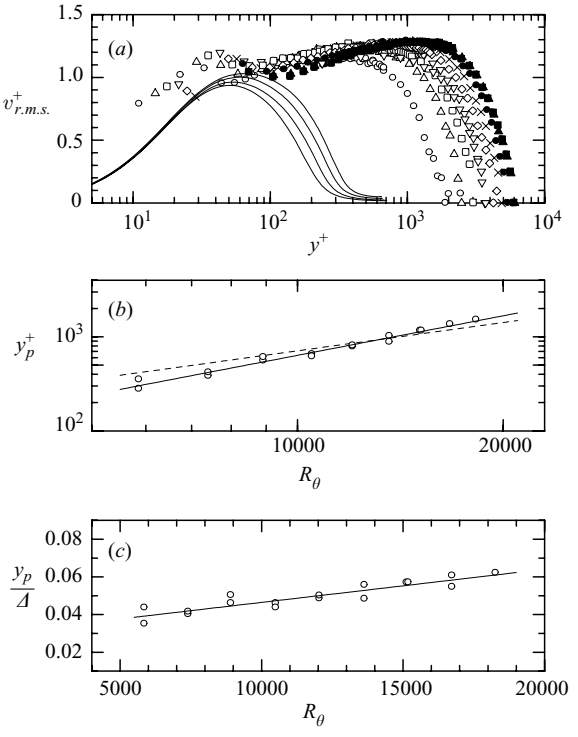


FIGURE 5. (*a*) Root-mean-square vertical velocity fluctuation calculated by equation (4.1). Same symbols as in figure 4 and solid lines are DNS by Skote (2001). (*b*) The peak position in terms of wall variables of $v^+_{r.m.s.}$ as a function of Reynolds number, and dashed line is the emperical relation $y^+_p = 0.071R_\theta$ by Fernholz & Finley (1996). (*c*) Peak position normalized with the Rotta–Clauser thickness.

below accessible measurement values. Here, $P_0^*$ is the mean pressure in the free stream and $v$ is the velocity fluctuation component normal to the plate. The root mean square (r.m.s.) distributions of the normal velocity are calculated from the above relation, using $P_0$ instead of $P_0^*$, and plotted in figure 5(*a*). The normalized fluctuation level, $\sqrt{\langle v^2\rangle}/u_\tau$, is slightly larger than expected from direct $v$-measurements. This discrepancy can, however, be explained by the uncertainty of $\Delta P_M \simeq O(10^{-1})$ Pa. Also, the calibration curve only reflects the relative errors. There is still an uncertainty in how accurately the mean static pressure is obtained with the Prandtl tube, as well as in the effect of the connecting plastic tube (see Appendix A.2). The profiles are similar to other direct measurements of $v_{r.m.s.}$ (cf. e.g. Österlund 1999). It seems that the maximum level is fairly independent of the Reynolds number when scaled by inner variables, which is shown in figure 6 where the X-wire probe data by Österlund are plotted for comparison. In figure 5(*b*) the peak position of $\sqrt{\langle v^2\rangle}/u_\tau$, denoted $y^+_p$, is plotted and its Reynolds number dependence illustrated. The dashed line is from Fernholz & Finley (1996), and represents $y^+_p = 0.071R_\theta$. If, however, this position is instead scaled with the Rotta–Clauser thickness it becomes fairly constant, only slightly increasing with Reynolds number (see figure 5*c*). Since the logarithmic region ends around $y/\Delta = 0.03$ it seems that the maximum of $v_{r.m.s.}$ is actually just outside the logarithmic region.

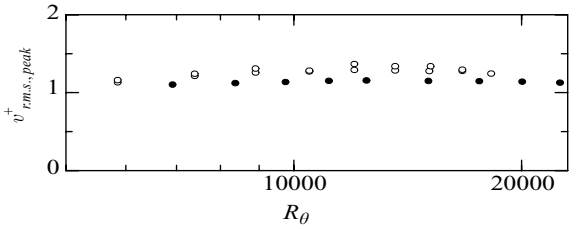


FIGURE 6. Maximum value of $v^+_{r.m.s.}$ as function of Reynolds number. ○, Data from figure 5(*a*); ●, data from Österlund (1999).

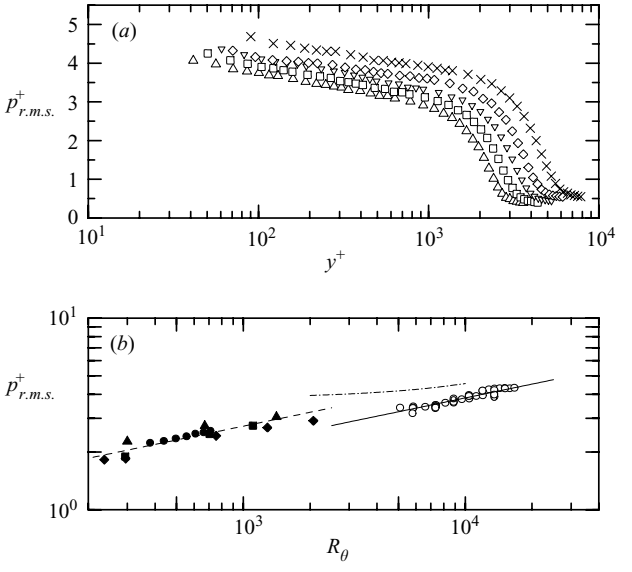


FIGURE 7. (*a*) Root-mean-square static pressure, normalized using inner variables: △, $R_\theta =$ 7420; □, $R_\theta = 8920$; ▽, $R_\theta = 10\,500$; ◇, $R_\theta = 12\,100$; ×, $R_\theta = 15\,200$. (*b*) Root-mean-square averaged in the log region plotted with ○ versus the Reynolds number. Solid symbols indicate the peak of $p^+_{r.m.s.}$ obtained by DNS: ●, Skote (2001); ■, Moser *et al.* (1999); ▲, Spalart (1988); ▼, Eggels *et al.* (1994); ◆, Abe *et al.* (2005). Solid and dashed lines are best fits for experiments and DNS, respectively. For both $p^+_{r.m.s.} \propto R_\theta^{0.24}$. Dash-dotted line corresponds to the relation $p^+_{r.m.s.,max} = 0.5\rho u^{+2}_{r.m.s.}$.

### 4.2. *Statistical feature of pressure fluctuation*

In this section, we analyse the static pressure fluctuations ($p_s$). Root-mean-square values and spectra are normalized by inner and outer variables, in order to investigate the Reynolds number scaling.

#### 4.2.1. *Root-mean-square values*

In figure 7(*a*) the r.m.s. of the pressure fluctuation is plotted versus the distance from the wall in the Reynolds number range $7420 \leqslant R_\theta \leqslant 15200$. These data have been corrected by removing the background noise according to equation (A 6). When normalized using inner variables, $p^+_{r.m.s.} \equiv p_{r.m.s.}/(\rho u_\tau^2)$, there is a clear $R_\theta$-dependence throughout the boundary layer. The inner r.m.s. peak $p^+_{r.m.s.,max}$ is, according to DNS results (Spalart 1988; Skote 2001), located around $y^+ \simeq 30$, and cannot be resolved in

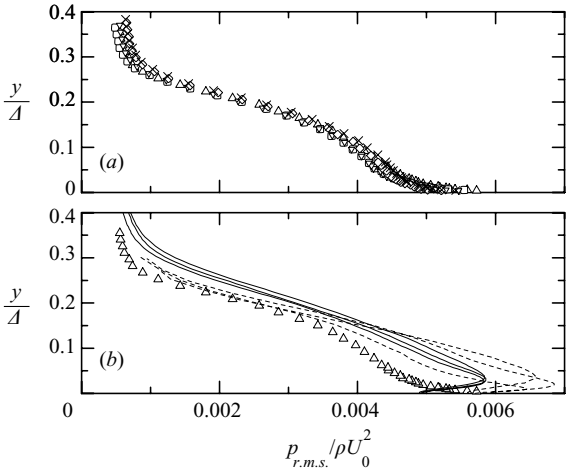


FIGURE 8. (*a*) Root-mean-square static pressure, normalized by twice the free-stream dynamic presssure. Symbols as in figure 7. (*b*) Similar distributions obtained with DNS. Solid lines are by Skote (2001) at $R_\theta = 450, 612, 716$, and dashed lines are by Spalart (1988) at $R_\theta = 300, 670, 1410$. Also plotted (△) are the experimental data for $R_\theta = 7420$.

these experiments due to physical probe interaction with the wall. With the type of probe used here one cannot get closer to the wall than $y^+ \approx 40$ and 90 for $R_\theta = 7420$ and 15200, respectively.

Direct numerical simulations show that the maximum value $p^+_{r.m.s.,max}$ increases as the Reynolds number increases. This Reynolds number dependence is shown in figure 7(*b*), where the channel flow data by Moser, Kim & Mansour (1999), Abe *et al.* (2005), the pipe flow data by Eggels *et al.* (1994) as well as the boundary layer data by Spalart (1988), Skote (2001), are included for comparison. The channel flow data show slightly lower $p^+_{r.m.s.,max}$ values than for the boundary layer. It is, however, not clear whether this small difference has a physical meaning or not. If these distributions are approximated by a power law, one finds $p^+_{r.m.s.,max} \propto R_\theta^{0.24}$.

The experimental data, plotted with circles in figure 7(*b*), have been obtained by averaging the $p^+_{r.m.s.}$ data in the log-region. Following the investigation by Österlund *et al.* (2000), the log-law region was evaluated to be $200 \leqslant y^+ \leqslant 0.15\delta^+$. A similar Reynolds number dependence as for the DNS peak value, $p^+_{r.m.s.} \propto R_\theta^{0.24}$, is experimentally confirmed here. It is also emphasized that this Reynolds number dependence is much stronger than that of streamwise intensity $u^+_{r.m.s.}$ or that of vertical velocity component $v^+_{r.m.s.}$ (see e.g. Österlund 1999).

On the other hand, when the pressure r.m.s. is normalized by outer variables, $\rho U_0^2$, and the distance from the wall with $\Delta$, the profiles more or less collapse on each other as shown in figure 8(*a*) for the same set of data as in figure 7(*a*). Figure 8(*b*) shows the DNS results by Skote (2001) ($R_\theta = 450, 612, 716$) and Spalart (1988) ($R_\theta = 360, 670, 1410$) in comparison with experiment. We can see a Reynolds number dependence when $R_\theta$ is small. The peak $p_{r.m.s.,max}/\rho U_0^2$ increases, and moves closer to the wall in terms of $y/\Delta$ as the Reynolds number increases. The results suggest that the Reynolds number dependence vanishes for $R_\theta > 7000$ and that $p_{r.m.s.}$ is scaled well by outer variables for high enough $R_\theta$.

The logarithmic friction law for zero-pressure-gradient turbulent boundary layers can be approximated (locally in $R_\theta$) by $u_\tau^2/U_0^2 \sim R_\theta^{-n}$, where a suitable choice for $n$ is around 0.2 in the range $500 < R_\theta < 15\,000$. This implies that the $R_\theta$ dependence

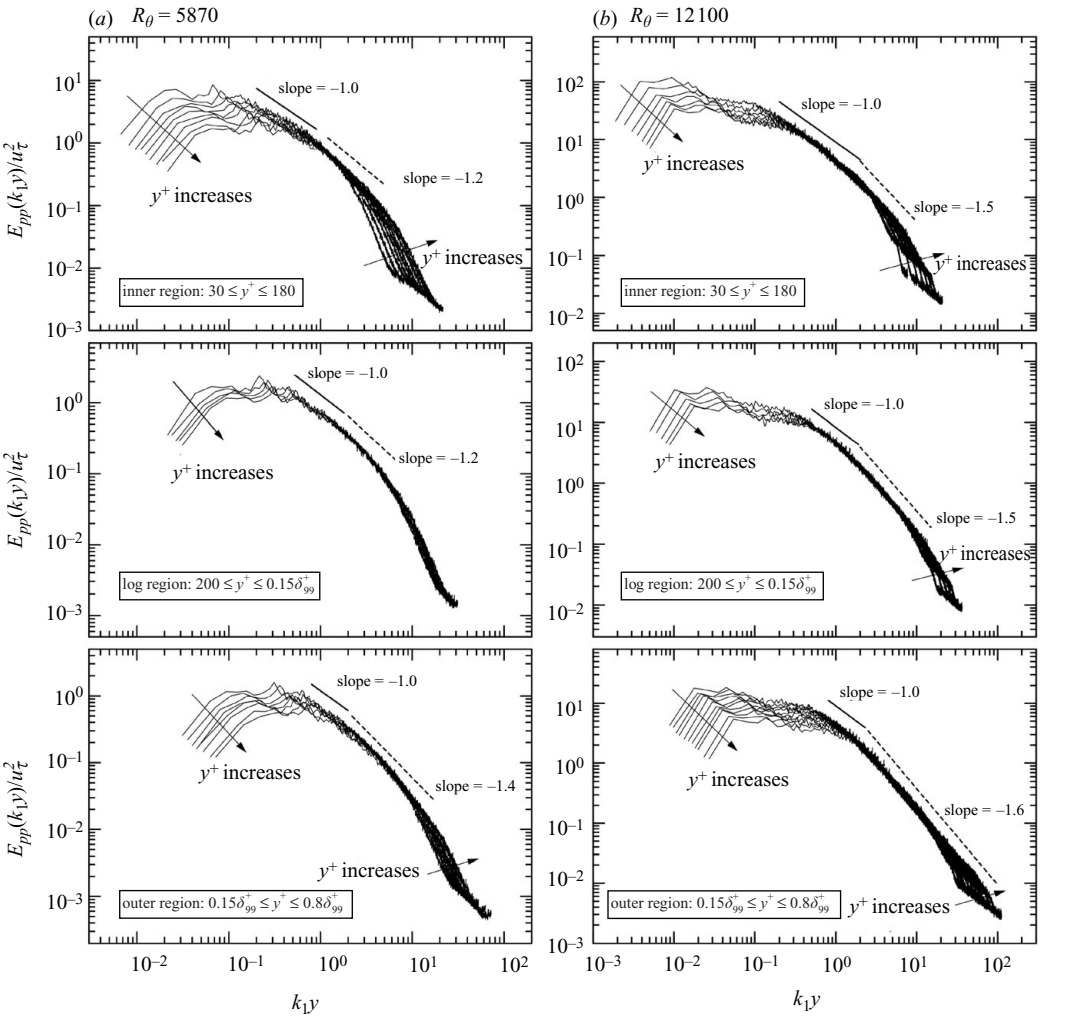


FIGURE 9. Static pressure spectra are plotted by inner-flow scaling: (*a*) $R_\theta = 5870$ and (*b*) $R_\theta = 12\,100$. The three rows correspond to the inner, the log, and the outer region which are defined as $y^+ < 180$, $200 \leqslant y^+ \leqslant 0.15\delta_{99}^+$, and $0.15\delta_{99} \leqslant y \leqslant 0.8\delta_{99}$, respectively. Here, $\delta_{99}$ is the boundary layer thickness taken as $U(\delta_{99}) = 0.99U_0$. The region of $k_1y$ where the solid power-law line has the slope $-1$ corresponds to overlap region I. The region of $k_1y$ where the dashed power-law line has the slope $\gamma_p$ corresponds to overlap region II.

on the pressure r.m.s. maxima using outer scaling should be expected to be weak, $p_{r.m.s.,max}/\rho U_0^2 \sim R_\theta^{0.04}$.

### 4.2.2. *Results on pressure spectra*

Figure 9 shows the pressure spectra in the inner scaling. They are classified into (1) an inner region, $y^+ < 180$; (2) a log region, $200 \leqslant y^+ \leqslant 0.15\delta_{99}^+$; and (3) an outer region, $0.15\delta_{99}^+ \leqslant y^+ \leqslant 0.8\delta_{99}^+$, for convenience. Here, $\delta_{99}$ is the boundary layer thickness taken as $U(\delta_{99}) = 0.99U_0$. We will study the Reynolds number dependence in the different regions. In the wall region for $R_\theta = 5870$, a power law with exponent approximately $-0.8$ is confirmed for $k_1y \leqslant 1$ and a steeper slope continues into the high-wavenumber region. As the Reynolds number increases to $R_\theta = 12\,100$, we find a $-1$ power law for $k_1y \leqslant 1$. This may be the overlap region I predicted by equation

(2.11). In the log region, the overlap region I becomes narrower than that of wall region, and it is difficult to find the $-1$ scaling in the outer region.

For sufficiently large Reynolds numbers we find a variation close to the $-1$ power law appearing in the static pressure spectrum. It is restricted to the low-wavenumber range $k_1 y < 1$ and becomes larger in the inner region. Notably, a similar $-1$ scaling region is seen in the wall pressure and this inverse power law becomes even clearer near the wall.

Panton & Linebarger (1974) solved numerically the rapid pressure term in equation (2.4) with some empirical results, and derived the $-1$ power law in the wall pressure spectrum. The rapid pressure term is dominant very close to the wall, say in the viscous sublayer, but it is not zero in the outer region. This is consistent with the observation that the $-1$ law region exists even in the outer region although its scaling range is very narrow.

In the overlap region II, following the Kolmogorov scaling, the spectrum has the $-7/3$ power law; however, the scaling regions next to I in the wall region exhibit a substantially lower value of the slope, $-1.2$ and $-1.5$ for $R_\theta = 5870$ and $R_\theta = 12\,100$, respectively. This power-law region becomes larger as the Reynolds number increases. It is also noted that the spectra approximately collapse over a large part of the wavenumber range. The spectra exhibit a rapid decrease for $k_1 y > 10$, which is thought to be close to the dissipation range. In the outer region, the other scaling regions with slope $-1.4$ for $R_\theta = 5870$ and slope $-1.6$ for $R_\theta = 12\,100$ are seen for $k_1 y \geqslant 3$. The spectra do not collapse for the low wavenumbers. Following these observations, we may conclude that the Kolmogorov scaling in overlap region II is not an appropriate description for the pressure fluctuation spectra. The failure of Kolmogorov scaling may be caused by the mean shear effect; this point will be discussed in more detail in the following subsection.

Other possible normalizations are represented by wall (inner) and outer variable scaling. Figure 10 shows the spectra at $y^+ \simeq 200$ normalized by inner and outer variables. Inner scaling appears appropriate for the high-frequency region ($f\nu/u_\tau^2 \geqslant 0.1$) and outer scaling for $f\Delta/U_0 \leqslant 10$. The power law with slope $-1.2$ is observed for $3 \times 10^{-3} \leqslant f\nu/u_\tau^2 \leqslant 8 \times 10^{-2}$. It is extended to lower frequencies as the Reynolds number increases. The insets show the spectra multiplied by the frequency in log-linear coordinates. In the inner scaling, for instance, the vertical axis of $(f\nu/u_\tau^2)E_{pp}/[\rho^2 u_\tau^2 \nu]$ is plotted in a linear coordinate against the frequency $f\nu/u_\tau^2$ in a logarithmic coordinate. The area below the curve corresponds to $(p_{r.m.s.}/\rho u_\tau^2)^2$. Similarly, the area is equal to $(p_{r.m.s.}/\rho U_0^2)^2$ for outer scaling.

In the inner scaling, the most significant contribution to the r.m.s. is from the range $10^{-4} \leqslant f^+ \leqslant 2 \times 10^{-1}$, but the low-frequency content increases as $R_\theta$ increases. Hence, $p^+_{r.m.s.}$ should increase with increasing Reynolds number. The pre-multiplied spectra collapse well when outer scaling is used. This means that $p_{r.m.s.}/\rho U_0^2$ is almost independent of Reynolds number for $y^+ = 200$.

At $y/\Delta = 0.065$ (figure 11, $y/\delta$ approximately 0.4) similar trends are confirmed. The power-law region in the pressure spectrum becomes wide and a clear power law with slope $-1.6$ is observed. We found that the static pressure fluctuation intensity inside the boundary layer scales with outer variables. Close to the wall on the other hand, say in the viscous sublayer, the outer scaling may not be appropriate. This point is discussed in relation to the scaling of wall pressure.

#### 4.2.3. *Reynolds number and anisotropic effect for pressure spectra*

Recent theoretical studies, numerical simulations, and experiments have revealed that the large-scale anisotropy caused by mean shear significantly affects the

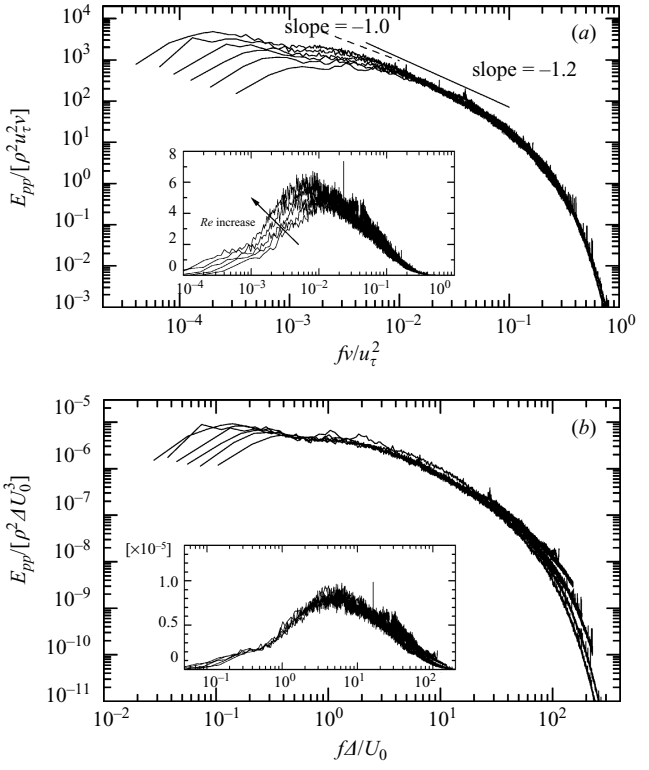


FIGURE 10. Static pressure spectra measured at $y^+ = 200$ for $R_\theta = 5870$, 7420, 8920, 10 500, 12 100, 15 200. The spectra are normalized by inner (*a*) and outer (*b*) variables. Insets in (*a*) and (*b*) show the multiplied spectra, $E_{pp}/[\rho^2 u_\tau^2 \nu] \times f\nu/u_\tau^2$ and $E_{pp}/[\rho^2 \Delta U_0^3] \times f\Delta/U_0$, respectively.

inertial-range statistics (Arad *et al.* 1998; Kurien *et al.* 2000; Shen & Warhaft 2000). In the case of two-dimensional boundary layers, the essential parameter characterizing the shear effect is the anisotropy or shear parameter ($S^*$) defined as

$$S^* = (\nu/\langle\varepsilon\rangle)^{1/2} S, \tag{4.2}$$

where $S$ is the mean velocity gradient, $S \equiv \mathrm{d}U/\mathrm{d}y$. $S^*$ is the ratio of the mean-shear time scale to the smallest eddy time scale $\tau_\eta \equiv (\nu/\langle\varepsilon\rangle)^{1/2}$. Although $S$ varies like $\simeq y^{-1}$ in the overlap region, $S^*$ behaves in a different way. Since $\langle\varepsilon\rangle$ behaves approximately as $y^{-1}$ in the log layer $S^*$ will decrease more slowly than $S$. We should, hence, expect $S^*$ to vary approximately as $y^{-1/2}$ with increasing distance from the wall (in the log layer).

If $S^*$ is small, the level of anisotropy created by the mean shear might also be expected to be small. There is some degree of uncertainty associated with the evaluation of $S^*$, because it is difficult to accurately determine the energy dissipation rate in laboratory experiments. Thus, the available data are restricted to the log region. The simplest method is to adopt the isotropic condition, $\langle\varepsilon\rangle_i \equiv 15\nu\langle(\partial u/\partial x)^2\rangle$, although this usually underestimates the true dissipation rate. Using the energy balance, the dissipation rate equals the difference between the production and diffusion terms. In a zero-pressure-gradient boundary layer, the dissipation term is approximately equal to the production term, i.e. $\langle\varepsilon\rangle_p \equiv -\langle uv\rangle(\partial U/\partial y)$. This relation

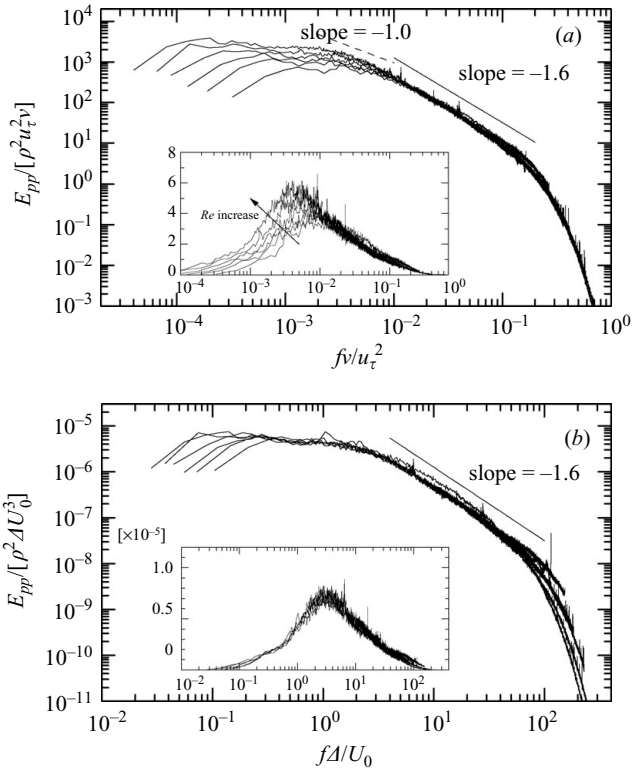


FIGURE 11. Static pressure spectra measured at $y/\Delta = 0.065$ for $R_\theta = 5870$, 7420, 8920, 10 500, 12 100, 15 200. The spectra are normalized by inner (*a*) and outer (*b*) variables. Insets in (*a*) and (*b*) show the multiplied spectra, $E_{pp}/[\rho^2 u_\tau^2 \nu] \times f\nu/u_\tau^2$ and $E_{pp}/[\rho^2 \Delta U_0^3] \times f\Delta/U_0$, respectively.

is usually adopted for convenience. However, the diffusion term is not negligible in the overlap region, thus $\langle\varepsilon\rangle_p$ overestimates the true dissipation. In this analysis, the dissipation rate is evaluated by plotting the normalized energy spectrum $E_{uu}(k_1)/[\langle\varepsilon\rangle^{1/4}\nu^{5/4}]$ against $k_1\eta$, and it is matched with the spectrum from a direct numerical simulation. In this way, the evaluated dissipation rate $\langle\varepsilon\rangle_e$ satisfies the condition $\langle\varepsilon\rangle_i < \langle\varepsilon\rangle_e < \langle\varepsilon\rangle_p$, and the normalized value $\langle\varepsilon\rangle_e L/u_{r.m.s.}^3$ is $O(1)$ in the overlap region, where $L$ is the integral length scale.

In the log region, both $S^*$ and $R_\lambda$ are plotted in figure 12, where the different symbols indicate the different $R_\theta$. Away from the wall, $S^*$ decreases but $R_\lambda$ increases; in other words, $S^*$ is a decreasing function of $R_\lambda$ for each $R_\theta$. The solid line (*a*) indicates the relation between $S^*$ and $R_\lambda$ at the lower end the of log region ($y^+ \simeq 180$) and the solid line (*b*) is the relation at the outer end of the log region ($y/\delta \simeq 0.15$). As the Reynolds number $R_\theta$ increases, $R_\lambda$ becomes larger and $S^*$ increases accordingly. Therefore, as plotted by the solid lines in the figure, large $R_\lambda$ is equivalent to large $S^*$, and $S^*$ cannot be small for large $R_\lambda$. This trend is contrary to the case of rough-wall boundary layers, Tsuji (2003), as plotted by the dashed line, in which $S^*$ is a decreasing function of $R_\lambda$, and the relation $S^* \propto R_\lambda^{-1}$ is satisfied in the overlap region for $4930 \leqslant R_\theta \leqslant 13\,100$.

In the log region, we may expect the Kolmogorov scaling with a $-7/3$ power-law behaviour. However, the measured spectra for several $R_\theta$ in the range of $150 < R_\lambda < 400$

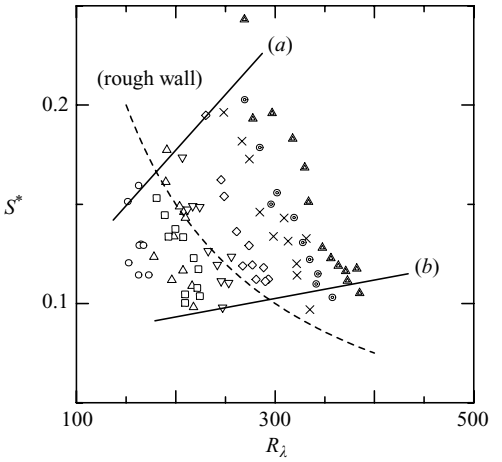


FIGURE 12. Relation between the shear parameter and the Reynolds number in the log region. Symbols indicate different Reynolds numbers. ○, $R_\theta = 5870$; △, $R_\theta = 7420$; □, $R_\theta = 8920$; ▽, $R_\theta = 10\,500$; ◇, $R_\theta = 12\,100$; ◎, $R_\theta = 13\,600$; ×, $R_\theta = 15\,200$; ⟁, $R_\theta = 16\,700$. The solid line (*a*) indicates the relation between $S^*$ and $R_\lambda$ at the lower end of the log region ($y^+ \simeq 180$) and solid line (*b*) at the outer end of the log region ($y/\delta \simeq 0.15$). Dashed line is the case of a rough-wall boundary layer (Tsuji 2003), in which the relation $S^* \propto R_\lambda^{-1}$ is satisfied in the overlap region for $4930 \leqslant R_\theta \leqslant 13\,100$.

did not follow the Kolmogorov scaling (not shown here). There is no evidence that the power-law exponent approaches $-7/3$, nor that the spectra collapse, so the Kolmogorov scaling is not satisfied. Compared with the result for the centreline of a turbulent jet (Tsuji & Ishihara 2003), which is close to the homogeneous isotropic condition, the pressure spectra in the shear flow widely differ from equation (2.7). This is likely to be due to the shear effect, which is present in the boundary layer case.

The exponent $\gamma_p$ evaluated by equation (2.8) is plotted against $R_\lambda$ and $S^*$ in figure 13. The second overlap region II, as discussed in figure 9, starts in $0.1 < k_1 y$ and might end before the dissipation range, $k_1\eta < 0.1$. The slope $\gamma_p$ is obtained by computing the local slope of the spectrum. In the logarithmic coordinates the part where the local slope is constant corresponds to the power-law region. We compute the exponent $\gamma_p$ by averaging the local slope. The error associated with this evaluation and other details are discussed in Appendix B. The symbols correspond to the different $R_\theta$. The dashed line is the result for $S^* = 0$ measured on the centreline of a turbulent jet. $\gamma_p$ is a decreasing function of $R_\lambda$ for a fixed value of $R_\theta$. For the present boundary layer case, however, $\gamma_p$ deviates substantially from the isotropic value of $-7/3$ even at high values of $R_\lambda$, and it also differs from the value obtained for the turbulent jet. This trend is better understood with the help of figure 13(*b*), where $\gamma_p$ is plotted as a function of $S^*$. $\gamma_p$ is less dependent on $R_\theta$ and is an increasing function of $S^*$. The solid line is the least-square fit,

$$\gamma_p = 0.8 \log_{10} S^* - 0.7. \tag{4.3}$$

Velocity spectra, on the other hand, have the scaling exponent $\gamma_u$ defined by

$$E_{uu}(k_1) = K_u' \langle\varepsilon\rangle^{1/4} \nu^{5/4} (k_1\eta)^{\gamma_u}, \tag{4.4}$$

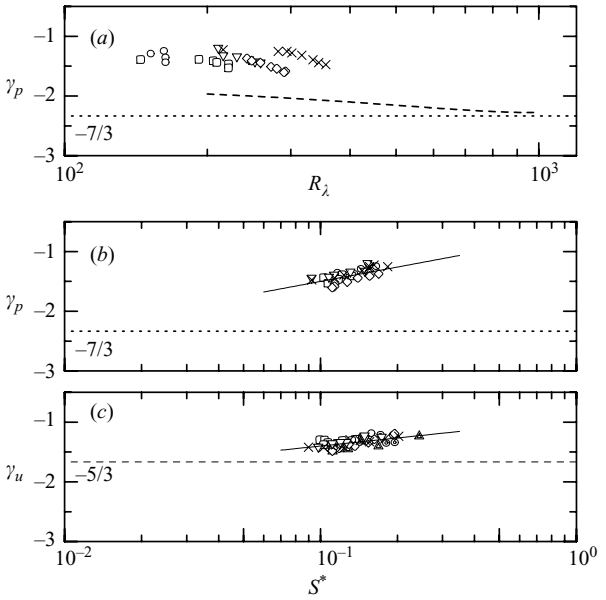


FIGURE 13. (*a*) The power-law exponent of the pressure spectrum in the log region against the Reynolds number. The dashed line is $S^* = 0$ measured in the centreline of a turbulent jet. (*b*) The power-law exponent of the pressure spectrum in the log region against the shear parameter. Solid line is equation (4.3) obtained by a least-square fit to the data. (*c*) The power-law exponent of the velocity spectrum in the log region against the shear parameter. Solid line is equation (4.5) obtained by a least-square fit to the data. Symbols indicate the different Reynolds numbers. ○, $R_\theta = 5870$; △, $R_\theta = 7420$; □, $R_\theta = 8920$; ▽, $R_\theta = 10\,500$; ◇, $R_\theta = 12\,100$; ◎, $R_\theta = 13\,600$; ×, $R_\theta = 15\,200$.

and in the log-law region the variation of $\gamma_u$ as a function of $S^*$ is given by

$$\gamma_u = 0.45 \log_{10} S^* - 0.95. \tag{4.5}$$

Thus, the exponents do indeed depart from the isotropic values $\gamma_p = -7/3$ and $\gamma_u = -5/3$ for large $S^*$. The data indicate that the shear effect is more significant for the pressure, that is, the pressure exponent changes more rapidly than that of the velocity. Extending these solid lines, local isotropy is expected to become realized for $S^* \simeq O(10^{-2})$. Hence, we conclude that local isotropy is not restored in the inertial range even if $R_\theta$ is $O(10^4)$. This is the reason why we cannot observe the Kolmogorov scaling in the overlap region II. In the present experiment we believe that the observed $\gamma_p > -7/3$ is mainly due to the fact that Reynolds number is too small for a given $S^*$, which causes the anisotropic contribution to dominate the pressure fluctuation. For a smooth wall it is not possible to increase $R_\lambda$ while keeping $S^*$ small in the overlap region. Therefore, local isotropic conditions may not be achieved in this region. One possibility to achieve local isotropy is to use a rough wall, thereby increasing the turbulence intensity near the wall.

### 4.3. *Statistical features of wall pressure*

In this section, we analyse the wall pressure fluctuations, and investigate Reynolds number scaling behaviour of root-mean-square values and spectra.

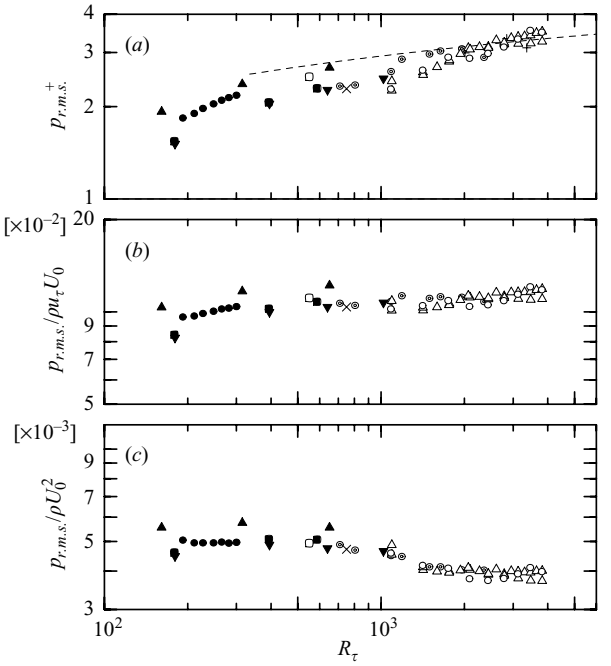


FIGURE 14. Root-mean-square wall pressure normalized by (*a*) inner scaling, (*b*) mixed scaling, (*c*) outer scaling, as a function of Reynolds number. ○, Present results (transducer); △, Present results (microphone); ●, Skote (2001) (DNS, boundary layer); ▲, Spalart (1988) (DNS, boundary layer); ■, Moser *et al.* (1999) (DNS, channel flow); ▼, Abe *et al.* (2005) (DNS, channel flow); □, Schewe (1983) (boundary layer, $d^+ = 19$); ×, Nepomuceno & Lueptow (1997) (pipe flow, $d^+ = 21$); ◎, Gravante *et al.* (1998) (boundary layer, $2 < d^+ < 27$); – – –, $(p^+_{r.m.s.})^2 = 6.5 + 1.86\ln(R_\tau/333)$ (Farabee & Casarella 1991).

### 4.3.1. *Root-mean-square values*

The wall pressure was measured by methods (1)–(3) mentioned in § 3. The amplitude difference and phase delay were corrected by the method mentioned in Appendix A.3. The r.m.s. of the measured wall pressure, where the background noise evaluated by equation (A 6) is removed, is plotted in figure 14. Previous results are plotted for comparison, but only data for which the pinhole has a sensitive diameter less than 30 viscous wall units ($d^+ < 30$) are shown. Here, the pressure fluctuations are normalized with inner, outer and mixed scaling. For the inner scaling, wall pressure r.m.s., $p^+_{r.m.s.}$, increases slowly with increasing Reynolds number. The relation given by Farabee & Casarella (1991), $(p^+_{r.m.s.})^2 = 6.5 + 1.86\ln(R_\tau/333)$, is also indicated as a dashed curve where the $R_\tau$-dependence term was evaluated by integrating the spectra in the inverse power-law region $100/R_\tau \leqslant \omega\nu/u_\tau^2 \leqslant 0.3$. The functional form $(p^+_{r.m.s.})^2 \propto \ln(R_\tau)$ was first proposed by Bradshaw (1967*a*) but from comparison with the experimental data it appears to underestimate the Reynolds number dependence. The behaviour of $p_{r.m.s.}$ normalized by outer variables is shown in figure 14(*c*) and is seen to decrease as the Reynolds number increases but appears to reach an asymptotic value for high $R_\theta$. The decreasing trend at moderate $R_\theta$ was also observed by Gravante *et al.* (1998). However, it is seen that by normalizing the pressure with the mixed scaling (figure 14*b*) we obtain an overall small variation of the normalized r.m.s. level, but for high $R_\theta$, it tends to increase slightly.

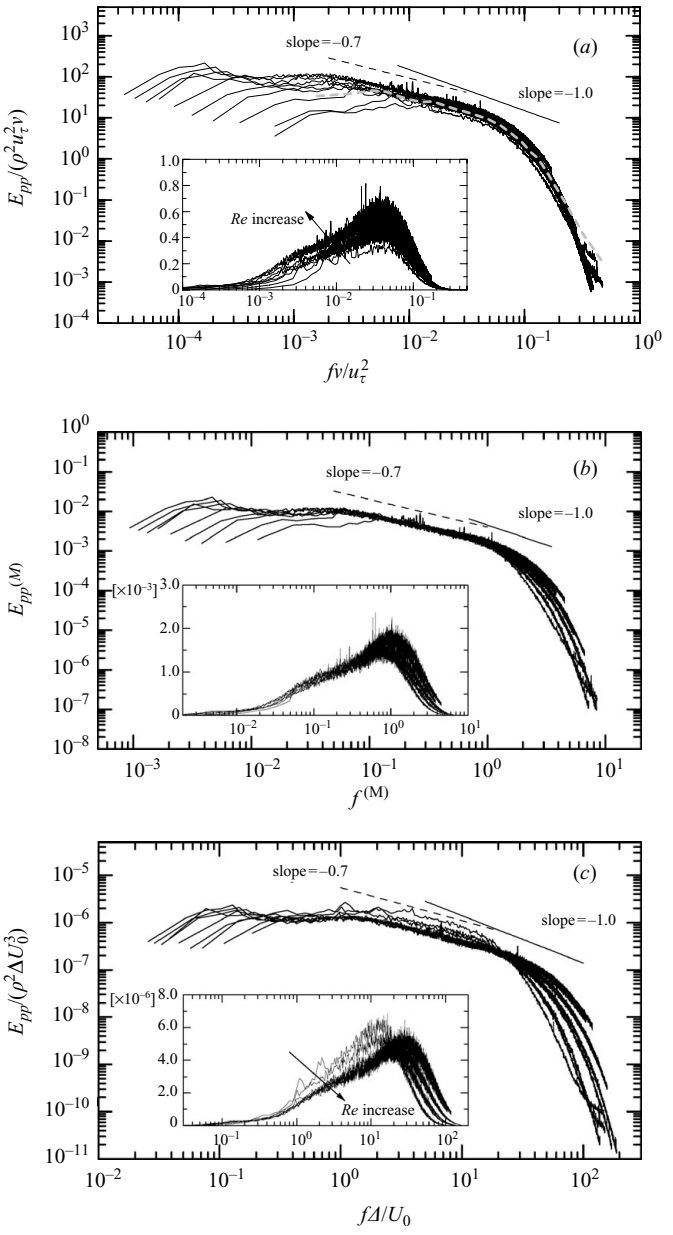


FIGURE 15. Wall pressure spectra normalized by (*a*) inner, (*b*) mixed and (*c*) outer variables in the range of $5870 \leqslant R_\theta \leqslant 16\,700$. The result of Gravante *et al.* (1998) at $R_\theta = 7076$ is plotted with a dashed line in (*a*) for comparison. Insets in (*a*), (*b*) and (*c*) show the multiplied spectra, $E_{pp}/[\rho^2 u_\tau^2 \nu] \times f\nu/u_\tau^2$, $E_{pp}^{(M)} \times f^{(M)}$ and $E_{pp}/[\rho^2 \Delta U_0^3] \times f\Delta/U_0$, respectively.

### 4.3.2. *Spectral scaling of wall pressure*

Figure 15 shows the wall pressure spectra normalized by inner, mixed, and outer variables. As is evident from equation (2.1), wall pressure is coupled to the velocity fluctuations throughout the boundary layer. It is generally believed that the

spectral contributions at high frequencies result from the velocity fluctuations in the wall region and the contributions at low frequencies are the result of large-scale velocity fluctuations that extend across the boundary layer. Separate non-dimensional parameters are therefore required for scaling the low- and high-frequency portions of the spectra. The scaling regions are usually classified as: (1) low-frequency range, spectra typically show the $f^2$ behaviour; (2) mid-frequency range; (3) universal range, with an $f^{-1}$ relation; and (4) high-frequency range. The wall pressure spectra normalized by inner variables are shown in figure 15(*a*). The high-frequency region of the spectra scale with inner variables, indicating that the wall region of the boundary layer is the dominant source of the high-frequency pressure fluctuations.

Bradshaw (1967*b*) predicted a region where spectra collapse on both inner and outer variables. This region exhibits an $f^{-1}$ behaviour, which can be associated with pressure sources in the logarithmic part of the boundary layer. Panton & Linebarger (1974) estimated the $-1$ power-law region to exist for Reynolds numbers, $R_\tau > 1000$. In the time–frequency spectrum, Farabee & Casarella (1986) presented the estimation of the overlap region as $100/(2\pi R_\tau) \leqslant f^+ \leqslant 0.3/2\pi$, which is realized for $R_\tau \geqslant 333$.

The current results show that a significant portion of the spectra exhibits a power-law behaviour, but with an exponent close to $-0.7$. This is observed over $0.002 \leqslant f^+ \leqslant 0.03$, for the highest $R_\theta$. It becomes narrower as the Reynolds number decreases. The spectrum measured by Gravante *et al.* (1998) for $R_\theta = 7076$ is shown by the dashed line. No extended $f^{-1}$ scaling region is explicitly evident in their data, either. We are led to assume that an overlap region with the $-1$ power of the spectrum slope is beyond the reach of laboratory measurements. Klewicki *et al.* (2005), on the other hand, demonstrated wall pressure measurements in a boundary layer developed over the salt playa of the Utah desert. A clear $-1$ power law behaviour was observed at $R_\tau \simeq O(10^6)$.

The spectra normalized by outer variables are shown in figure 15(*c*). The low-frequency range for $0.2 \leqslant f\Delta/U_0 \leqslant 10$ is scaled well in the sense that there is no Reynolds number dependence. The asymptotic behaviour of normalized pressure variance, $p_{r.m.s.}/\rho U_0^2$, is coupled to the scaling of this low-frequency range, since the most energetic contributions to $p_{r.m.s.}$ are associated with $f\Delta/U_0 \leqslant 20$.

The insets show the spectra multiplied by the frequency as in figure 10. Outer scaling only collapses the high-$R_\theta$ spectra in the low-frequency region. Mixed scaling gives the least dependence on the Reynolds number if one considers the overall collapse, but inner scaling gives the best collapse in the high-frequency regime. Wall pressure spectra illustrate well the influence on the near-wall region, not only from the small-scale, near-wall motions, but also from the large-scale motions that extend over a substantial part of the boundary layer. The scaling behaviour with an approximate overall collapse with mixed scaling reflects this interaction process between the outer flow and the flow in the near-wall region. In this context, note that Alfredsson & Johansson (1984) found that the governing time scale for the frequency of occurrence of shear layer structures in the near-wall region to be a mixture (the geometric mean) of inner and outer time scales.

In comparison with the static pressure spectra (figure 9), the overlap region II where the spectra show a slope of $-1.2$ matches partly the $-0.7$ power law region in wall pressure. When the Reynolds number becomes large enough, the former region is expected to exhibit a $-7/3$ power law and the latter a $-1$ slope. Several researches (e.g. Schewe 1983; Farabee & Casarella 1991; Gravante *et al.* 1998) have predicted the existence of a $-7/3$ power law of the wall pressure spectrum, but there

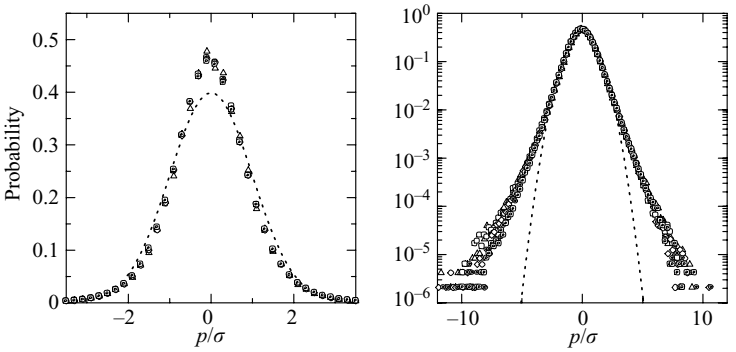


FIGURE 16. Probability density function of wall pressure fluctuation. Symbols indicate different Reynolds numbers. Dotted line is Gaussian. △, $R_\theta = 5870$; □, $R_\theta = 7420$; ◇, $R_\theta = 10\,500$; ◎, $R_\theta = 13\,600$; ⊡, $R_\theta = 16\,700$.

is no indication of such behaviour in the present data or in the data of an atmospheric boundary layer (Klewicki, Perkins & Metzge 2005). These experimental facts may indicate that a $-7/3$ power law might not be realized in the wall pressure spectra even for high-Reynolds-number flows.

### 4.4. *Probability density function of $p_s$ and $p_w$*

The probability density function (PDF) of the wall pressure fluctuations $p_w$ is shown in figure 16. The pressure is normalized by its standard deviation $\sigma$. Around the centre $p/\sigma \simeq 0$, the probability is larger than the Gaussian distribution. In the range $5870 \leqslant R_\theta \leqslant 16\,700$, PDFs show little Reynolds number dependence. In the tail parts, the PDF shape deviates significantly from Gaussian and it is closer to an exponential form. The negative tail part shows a weak Reynolds number trend that is somewhat more distinct than for the positive side. The skewness is about $-0.05$ for $R_\theta = 5870$ but gradually increases up to 0.09 for $R_\theta = 16700$. Flatness is monotonically decreasing from 5.2 to 4.5. The probability distribution of wall pressure by Schewe (1983) for the smallest transducer ($d^+ = 19$) shows an asymmetry such that the events with large negative amplitude occur more frequently, hence are associated with a negative skewness. This asymmetry is discussed further in a later section. The relatively high value of the flatness signifies the existence of rare high-amplitude wall pressure peaks associated with the tails of the PDF.

Figure 17 shows the static pressure PDFs at several locations across the boundary layer ($0.0074 \leqslant y/\Delta \leqslant 0.163$) at $R_\theta = 10\,500$. Around the centre, the maximum probability occurs for a slightly positive $p$-value. The maximum is larger than the Gaussian value, and the dependence on the location $y/\Delta$ seems to be weak. In the tail parts, the negative side deviates significantly from Gaussian, which is similar to the PDF of $p_w$. It is, however, noted that the positive side increases as $y/\Delta$ decreases. That is, the positive tail deviates from the Gaussian value as the wall is approached. The wall pressure PDF at the same Reynolds number is indicated by the solid line. The negative tail of the wall pressure coincides with the negative tails of the static pressure PDFs. The positive tails of static pressure tend to asymptote towards the positive tail of the wall pressure as $y/\Delta$ goes to zero.

For comparison, we also plot the PDF measured on the centreline of a free jet by Tsuji & Ishihara (2003), indicated by the dashed line. This PDF bears a striking resemblance to the PDF of homogeneous isotropic turbulence. Around the centre

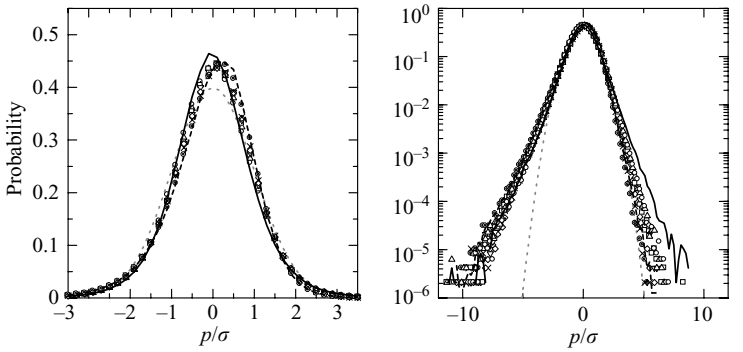


FIGURE 17. Probability density function of static pressure fluctuation at $R_\theta = 10\,500$. Symbols indicate different positions from the wall. Solid line is the PDF of wall pressure at the same Reynolds number. Dashed line indicates the PDF measured on the centreline of a jet at $R_\lambda = 320$ (Tsuji & Ishihara 2003). Dotted line is Gaussian. ○, $y/\Delta = 0.0074\,(y^+ = 104.9)$; △, $y/\Delta = 0.013\,(y^+ = 188.8)$; □, $y/\Delta = 0.024\,(y^+ = 333.5)$; ▽, $y/\Delta = 0.036\,(y^+ = 503.7)$; ◇, $y/\Delta = 0.059\,(y^+ = 839.5)$; ×, $y/\Delta = 0.109\,(y^+ = 1553.1)$; ◎, $y/\Delta = 0.163\,(y^+ = 2392.5)$.

region, the peak is higher than for the Gaussian and the peak is located on the positive pressure side. It is strikingly similar to the static pressure PDFs in the outer region of the boundary layer. In the negative tail part, this PDF matches those of both static pressure $p_s$ and wall pressure $p_w$ in the boundary layer, but in the positive tail, the PDF from the jet is closer to the Gaussian distribution. We may conclude that the shear effect predominantly appears for positive pressure fluctuations, and causes the positive tail to deviate from the Gaussian distribution.

According to the decomposition of $p$ in equation (2.3), the mean velocity gradient is included in the source term of the rapid pressure $p^{(r)}$, which means that $p^{(r)}$ is directly affected by the shear. It may be assumed that the positive large-amplitude pressure fluctuations observed near the wall are associated with the rapid pressure term, since we have observed that the positive PDF tail is very close to Gaussian in the case of $\partial U/\partial y = 0$ (homogeneous isotropic flow). The larger the shear, the more significant deviation from Gaussian behaviour is observed.

The higher-order moments, skewness and flatness, of the pressure were computed and were found to be approximately $-0.35$ and 4.6, respectively, in the log region. Furthermore, their Reynolds number dependence was found to be small. Thus the pressure PDF may exhibit a self-similar shape in the log region if the fluctuations are normalized by their standard deviation. For the streamwise velocity fluctuation, we have already documented the invariant PDF shapes in the overlap region (Lindgren, Johansson & Tsuji 2004; Tsuji, Lindgren & Johansson 2005*b*). It is interesting that not only velocity but also pressure fluctuations may have a universal PDF shape in the overlap region.

### 4.5. *Correlation between static and wall pressure*

The correlation between wall pressure and static pressure is plotted in figure 18 for different Reynolds numbers. The background noise evaluated by equation (A 6) is removed from the measured data. One may conclude first that a positive correlation is observed across the entire boundary layer. Secondly, there is no significant Reynolds number dependence for $R_\theta > 7000$ when the distance from the wall is scaled by $\Delta$. The same correlation along the normal direction was computed by Kim (1989, figure 15*a*), in which the positive correlation remains even on the channel centreline. He also

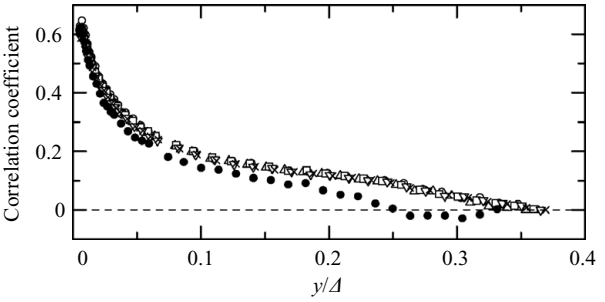


FIGURE 18. Correlation coefficient between wall pressure and static pressure throughout the boundary layer. Symbols indicate the experimental results: ●, $R_\theta = 5870$; △, $R_\theta = 7420$; □, $R_\theta = 8920$; ▽, $R_\theta = 10\,500$; ◇, $R_\theta = 12\,100$; ×, $R_\theta = 13\,600$.

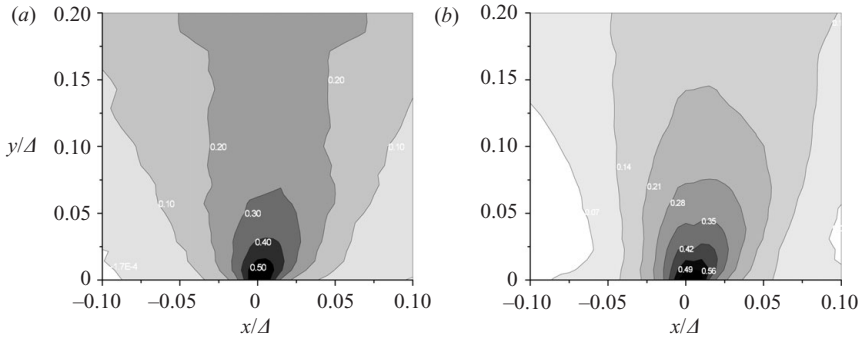


FIGURE 19. Contour plot of the correlation coefficient between wall pressure and static pressure in the $x$, $y$-plane. ($a$) $R_\theta = 5870$, ($b$) $R_\theta = 13\,600$.

noted that the correlation length for the pressure along the normal direction is much larger than for the velocity quantities. Here, we cannot compare quantitatively with the result by Kim, because the flow field is different. However we emphasize that the positive correlation remains even far from the wall.

There are many reports on the correlation of velocity and wall pressure fluctuations. Panton *et al.* (1980) made wall pressure as well as velocity measurements inside and outside a turbulent boundary layer developed on the fuselage of a glider airplane. They found that the velocity fluctuations maintained a strong correlation with the wall pressure even where the r.m.s. value of the velocity in the non-turbulent region was less than or equal to 0.45 %. Kobashi, Komoda & Ichijo (1984) and Kobashi & Ichijo (1986) repeated the wall pressure–velocity correlation measurements. They classified at least two kinds of wall pressure fluctuations. One is associated with the large-scale structures that originate from the outer part of the boundary layer. The other is the small-scale fluctuations (typically called sweep, ejection, and burst) which are limited to the wall region. These experimental results indicate that the positive correlation between $p_s$ and $p_w$, which remains outside the boundary layer, may be attributed to the large-scale structures.

Contours of the two-point correlation between $p_s$ and $p_w$ as a function of streamwise and normal separation are plotted in figure 19. Using the Taylor hypothesis, the streamwise distance is computed by the relation $x = -\tau U(y)$, where $\tau$ is a time lag and $U(y)$ is the local mean velocity. It is noted that the maximum correlation is restricted to the near-wall region, but the positive correlation extends far from the wall. This shows clearly that two different types of events contribute the wall pressure

as pointed out by Kobashi *et al.* (1984) and Kobashi & Ichijo (1986). Kim also noted that this correlation extends far in the wall-normal direction in channel flow (Kim 1989, figure 13*a*).

Abe *et al.* (2005) found large-scale structures which become elongated in the $z$-direction with a streamwise spacing of about $2\delta$. They are located around the channel centre but have a substantial correlation with the wall pressure.

By conditional averaging of the wall pressure and the streamwise velocity at various wall distances, Johansson, Alfredsson & Kim (1991) showed that the positive wall pressure peaks are related to shear layers in the buffer region and are associated with the rapid source term. The dominant contribution from the rapid term is restricted to the buffer region. For negative wall pressure peaks, however, no coupling to the shear layers was found. The relationship between the wall pressure and shear layers detected by the VITA technique at various wall distance was also investigated by Tanifuji *et al.* (1986) in pipe flow, who confirmed that the shear layers in the buffer region are major contributors to the sharp positive wall pressure peaks. This was further confirmed by Jeong *et al.* (1997) from a somewhat different point of view.

A more general definition of such small-scale high-vorticity coherent structures (CS) was given by Kida & Miura (1998). These structures exist generally in turbulence, and it is noted that the pressure becomes negative in the centre of the CS (vortex filaments). The negative pressure tail is likely to be associated with such small-scale CS, partly since the negative tail form is almost independent of the flow field as indicated in figure 17.

Although the present measurements cannot reach into the buffer region, we may compute the contours of $p_s$ conditioned by large positive and negative wall pressure peaks which are larger than four times the r.m.s. values. Referring to figure 15, we divide the frequency range of $p_s$ into three parts: (*a*) a low-frequency range before the start of the $-0.7$ power-low region, $f^+ \leqslant 2 \times 10^{-3}$; (*b*) a frequency range up to the end of the $-0.7$ power law region, $f^+ \leqslant 2 \times 10^{-2}$; (*c*) a high-frequency range, $f^+ \geqslant 2 \times 10^{-2}$. The low-frequency range (*a*) of $p_s$ is independent of large wall pressure peaks. A weak correlation is observed in the range of (*b*) across the boundary layer. Both positive and negative peaks have a similar correlation to $p_s$. On the other hand, wall pressure spikes have a strong correlation with the frequency range (*c*). Although restricted to the region below the log region, the negative peaks indicate a stronger correlation with $p_s$. Also, the ratios $r.m.s._p^+/r.m.s.$ and $r.m.s._p^-/r.m.s.$, where $r.m.s._p^+$ indicates the contribution from positive pressure peaks and $r.m.s._p^-$ from negative peaks, are computed. We can say that the large-amplitude wall pressure event has a strong correlation at least up to the end of the log region. This indicates that the pressure correlation extends further than the velocity correlation.

Schewe (1983) estimated the location of the effective source terms for the pressure in terms of the distance from the wall. He found them to be centred at $y^+ = 21$ where the mean velocity is equal to the propagation velocity of pressure at the wall. In the DNS by Kim (1989), it corresponds to $y^+ \simeq 23$ with $U = 13u_\tau$. Kim (1989) also found that this approximately coincides with the location where the mean-square source term has its maximum. It is interesting to note that Schewe's estimation approximately matches the location of the maximum of the mean-square source term. If we assume that the dominating contributions to this source term are associated with vortex-like structures (Kim 1989), it would suggest that the most intense wall pressure fluctuations can be connected to vortex structures present near $y^+ \simeq 20$. This is consistent with Alfredsson, Johansson & Kim (1988) who reported that a large pressure peak is typically found underneath the internal shear-layer structure responsible for much of the turbulence production in the wall region.

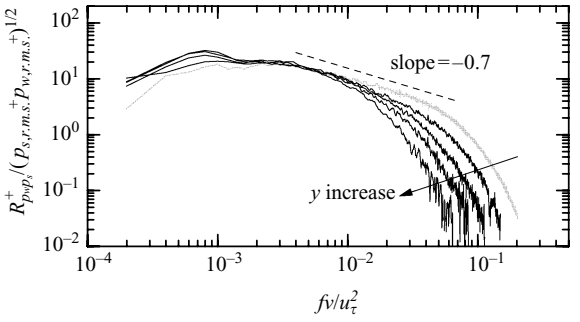


FIGURE 20. Cross-spectra of wall pressure and static pressure for $R_\theta = 7420$ at $y^+ = 57, 100, 171, 285$. Grey line indicates the wall pressure spectra for $R_\theta = 7420$.

Here, we focus on the source term associated with the $-1$ power-law region. Panton & Linebarger (1974) concluded that such a source term is predominantly located in the log region and outer part of the buffer layer: $33.2 \leqslant y^+$, $y/\delta \leqslant 0.2$. In figure 20, the cross-spectra defined by

$$\langle p_w p_s \rangle = \int_0^{+\infty} R_{p_w p_s}(f)\,\mathrm{d}f. \tag{4.6}$$

are plotted at different locations from the wall. The Reynolds number is $R_\theta = 7420$ and the upper end of log region is $y^+ \simeq 300$. The wall pressure spectrum at the same Reynolds number is plotted for comparison. In this experiment the Reynolds number is not high enough to generate a $-1$ power law. The slope is approximately $-0.7$. Small-scale correlation associated with $f^+ \geqslant 2\times10^{-2}$ rapidly decreases as the distance from the wall increases. The contribution to the $-0.7$ power law is seen to originate from positions up to the end of the log region. Bradshaw (1967*a*) assumed that if $y_k$ is the distance from the wall at which the mean velocity is equal to the convective velocity for a given wavenumber $k_1$, then $k_1 y_k \simeq 1$. This is approximately satisfied in the present cross-spectra. At the upper end of the log region ($y^+ \approx 300$), the normalized wavenumber is $k_1^+ \simeq 1/y^+ = 1/300$, and the corresponding frequency becomes $f_1^+ = U_c/(2\pi)k_1^+ \simeq U_c/(2\pi)/y^+$. Although the convective velocity $U_c$ is not constant but a function of $k_1$, assuming the relation $U_c = 0.7U_0$ (Kim 1989), we have $f_1^+ \approx 3.3\times10^{-3}$. This corresponds well to the lower end of $-0.7$ power-law region in figure 20.

### 4.6. *Velocity and pressure correlation*

Streamwise velocity and pressure fluctuations were measured simultaneously in one series of measurements. First, we consider the ratio $C_1 = p_{r.m.s.}/(\rho u^2_{r.m.s.})$. Using a quasi-normal assumption the ratio $C_1$ can be derived theoretically. It was estimated by Hinze (1975) to be about 0.7 and by Batchelor (1951) to be $C_1 \approx 0.58$. Recent DNS data for homogeneous isotropic turbulence suggest $0.8 \leqslant C_1 \leqslant 1.0$ for $R_\lambda < 300$ but a weak dependence on Reynolds number has been observed in isotropic turbulence (Gotoh & Fukayama 2001; Vedula & Yeung 1999; Cao *et al.* 1999). This ratio was measured experimentally by Tsuji & Ishihara (2003) and Tsuji & Ishihara (2006) on the centreline of a free jet, where $C_1$ is about 0.7 for low Reynolds numbers. In the boundary layer, plotted in figure 21, $C_1$ is found to be dependent on the distance from the wall. The ratio is unity in the overlap region, but rapidly increases in the wake region. In comparison with DNS by Skote (2001), plotted by the solid line, the $C_1$-values match in the overlap region. The ratio takes the smallest value at $y^+ \simeq 10$, and it also rapidly increases close to the wall.

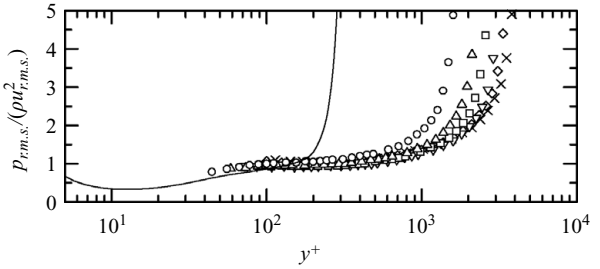


FIGURE 21. Root-mean-square static pressure normalized by the intensity of streamwise velocity fluctuation. Solid line is DNS by Skote (2001) at $R_\theta = 716$. Symbols indicate the experimental results: ○, $R_\theta = 5870$; △, $R_\theta = 7420$; □, $R_\theta = 8920$; ▽, $R_\theta = 10\,500$; ◇, $R_\theta = 12\,100$; ×, $R_\theta = 13\,600$.

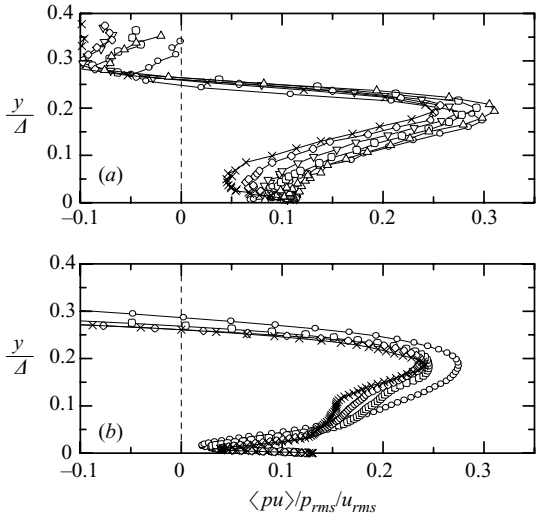


FIGURE 22. Correlation coefficient between streamwise velocity and pressure throughout the boundary layer. (*a*) Experimental results: ○, $R_\theta = 5870$; △, $R_\theta = 7420$; □, $R_\theta = 8920$; ▽, $R_\theta = 10\,500$; ◇, $R_\theta = 12\,100$; ×, $R_\theta = 13\,600$. (*b*) DNS by Skote (2001). ○, $R_\theta = 383$; □, $R_\theta = 538$; ◇, $R_\theta = 612$; ×, $R_\theta = 712$.

The maximum $p^+_{r.m.s.}$ is around $y^+ = 30$, and the ratio $p_{r.m.s.}/\rho u^2_{r.m.s.}$ is about 0.5 at this location as indicated in figure 21. We can estimate $p_{r.m.s.,max}$ using relation $p^+_{r.m.s.,max} = 0.5\rho u^{+2}_{r.m.s.}$ if the maximum of $u^+_{r.m.s.}$ is evaluated to be $u^+_{r.m.s.,max} = 2.65 + 2.5R_\theta/10^5$ for $2000 \leqslant R_\theta \leqslant 10\,000$ (Österlund 1999). $p^+_{r.m.s.,max}$ estimated in this way is plotted in figure 7 as a dash-dotted line. The values fall close to the extension of the low-Reynolds-number DNS results.

The correlation between the static pressure and the streamwise velocity fluctuations, $\langle pu \rangle/(p_{r.m.s.}u_{r.m.s.})$, is plotted in figure 22. Three significant features can be seen. First, the correlations show a local minimum value at $y/\Delta \simeq 0.05$. Secondly, the maximum correlation is located around the boundary layer thickness, $y \simeq 0.2\Delta$ ($\Delta \approx 6\delta$, $\Rightarrow$ $y \simeq 1.2\delta$). Thirdly, the correlation becomes negative in the free-stream region. These trends are also clearly seen in the joint probability density function of $p_s$ and $u$ (figure 23). In the overlap region (at $y/\Delta = 0.095$), the contours form an elliptical distribution and the highest probability exists in the first quadrant. This tendency

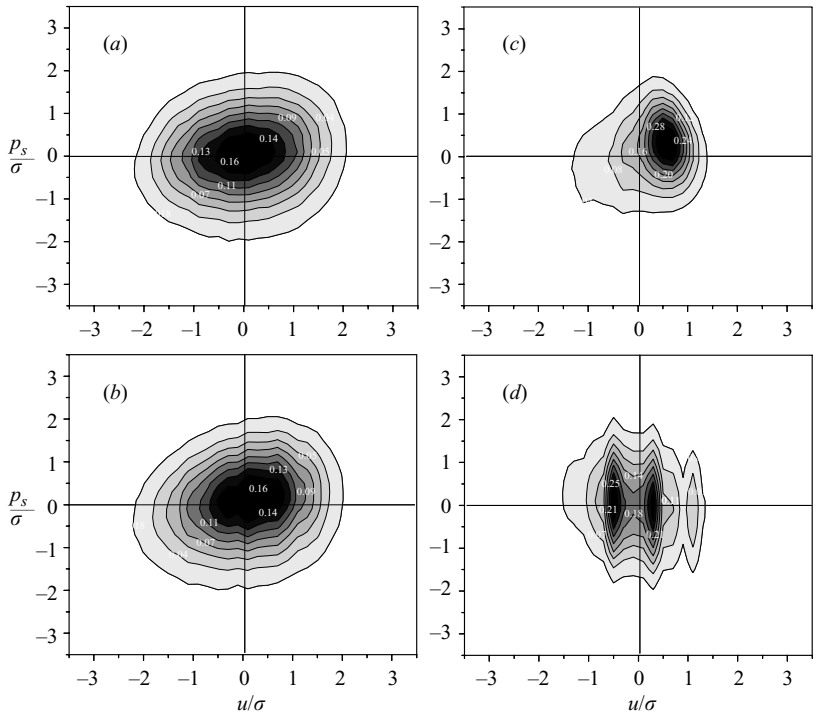


FIGURE 23. Joint probability density function for static pressure and streamwise velocity fluctuation at $R_\theta = 8920$. Axes are normalized by their standard deviations. (*a*) $y/\Delta = 0.033$, (*b*) $y/\Delta = 0.095$, (*c*) $y/\Delta = 0.20$, (*d*) $y/\Delta = 0.27$.

becomes strong at $y/\Delta = 0.20$ where the correlation is a maximum. The most probable events are positive $u$ fluctuations accompanied with positive $p_s$. In the free-stream region, the contour is distorted because the velocity fluctuations become very small. This indicates a negative correlation on the whole, which may be understood from the Bernoulli equation. It is noted that these three features are also observed in the DNS by Skote (2001).

It may be difficult to explain the reason for the positive correlation between $p_s$ and $u$ within the limits of the present experiment. But we should note the negative tail of $p_s$ as discussed in § 4.4. This is a significant characteristic of the pressure. A large negative pressure fluctuation is observed not only in homogeneous isotropic flow but also in shear flows. The tail part may be emphasized by taking the logarithm of PDF (the graph is not shown here), which reveals that in the overlap region (at $y/\Delta = 0.033$) negative large pressure has a correlation with negative velocity fluctuations, i.e. the third quadrant is dominating over the first quadrant. This trend becomes clearer at $y/\Delta = 0.20$.

## 5. Summary and Conclusions

In this experiment, both static pressure and wall pressure fluctuations are measured in high-Reynolds-number turbulent boundary layers. The main results may be summarized as follows:

(i) The root mean square of vertical velocity component $\sqrt{\langle v^2 \rangle}$ is evaluated using the mean pressure distribution with (4.1). The profile agrees reasonably well with the result obtained by direct $v$-component velocity measurements.

(ii) The distribution of the r.m.s. pressure fluctuations normalized by inner variables, $p^+_{r.m.s.}$, shows a Reynolds number dependence. If $p^+_{r.m.s.}$ is averaged within the log region, it is approximated by the power law $p^+_{r.m.s.} \propto R_\theta^{0.24}$. DNS shows that $p^+_{r.m.s.}$ has its maximum $p^+_{r.m.s.,max}$ at $y^+ \simeq 30$ and that the Reynolds number dependence is $p^+_{r.m.s.,max} \propto R_\theta^{0.24}$. These Reynolds number dependences are much stronger than those of streamwise or vertical velocity components. On the other hand, if the pressure r.m.s. is normalized by the outer scale $U_0$ and the distance from the wall by $\Delta$, the profile is almost independent of Reynolds number for $R_\theta \gtrsim 7000$.

(iii) Static pressure spectra show a $-1$ power-law slope in the low-wavenumber region but the Kolmogorov scaling with a predicted $-7/3$ power-law is not observed. This may be because the Reynolds number is not large enough to achieve local isotropy for a given shear rate $S^*$. Local isotropy may be expected at $S^* = O(10^{-2})$, but this condition cannot be realized in a smooth-wall boundary layer. In the log region, not only pressure r.m.s. but also pressure spectra at low wavenumbers collapse fairly well when they are normalized by $U_0$ and $\Delta$.

(iv) Root-mean-square values of wall pressure normalized by inner variables are an increasing function of $R_\theta$. Normalization by mixed scaling gives an overall small variation of the normalized $p_{r.m.s.}$. When r.m.s. is normalized by outer scales, it decreases gradually and appears to asymptote towards a constant value $p_{r.m.s.}/(\rho U_0^2) = 0.004$ for $R_\theta > 7000$. Therefore, both static and wall pressure r.m.s. become approximately constant when they are normalized by outer scales for sufficiently high Reynolds numbers.

(v) Spectra of wall pressure indicate a $-0.7$ power-law region but a $f^{-1}$ scaling region is not evident. Cross-correlation spectra between static and wall pressure show that the source term associated with this spectral region originates from positions up to the end of the log region.

(vi) The correlation between static and wall pressure is positive across the entire boundary layer, and there is no significant Reynolds number dependence for $R_\theta \geqslant 7000$ when the distance from the wall is scaled with $\Delta$. Two-point correlations show that the area of high correlation is restricted to the near-wall region, but a low positive correlation extends far in the normal wall direction. This indicates that two different kinds of events contribute to the wall pressure statistics. Joint probability density functions support this result and show that positive correlation is due to the large-amplitude positive and negative pressure fluctuations of both wall pressure and static pressure near the wall.

(vii) The ratio $p_{r.m.s.}/\rho u^2_{r.m.s.}$ was found to be of the order of one in the inner and overlap regions. The correlation between the pressure and streamwise velocity shows local minimum and maximum values at $y/\Delta \simeq 0.05$ and $y/\Delta \simeq 0.2$, respectively. In the outer region, $y/\Delta > 0.25$, the correlation becomes negative, which can be understood from potential flow arguments. These trends are also observed in DNS.

Financial support from the Japan Society for the Promotion of Science, the Royal Academy of Sciences, and the Swedish Research Council are gratefully acknowledged. Furthermore, we wish to thank Dr M. Skote and Dr H. Abe for fruitful discussions and providing DNS results for comparison. Finally, we wish to thank Mr M. Gällstedt at KTH Mechanics for his assistance in the workshop.

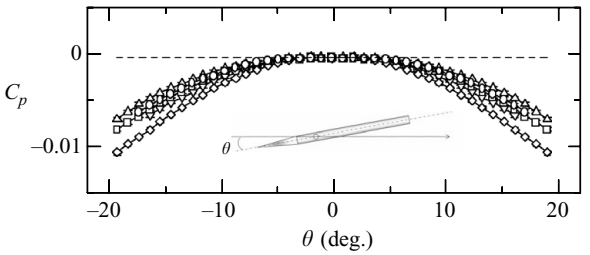


FIGURE 24. Yaw angle effect for various static pressure probes. For symbols see table 2.

## Appendix A. Calibration of static pressure probe

### A.1. *Yaw angle effect*

As described in § 3.1 the pressure sensor is aligned with the probe-body axis, which during the experiments is aligned with the mean flow direction implying that there is a small angle with the plate. In a preliminary investigation the yaw angle effect on the measured pressure between the pressure probe and the mean flow direction was studied. This was done by rotating the probe $-20^\circ \leqslant \theta \leqslant +20^\circ$ in the potential core of a round jet, which had an initial velocity of $U_J = 10\,\mathrm{m\,s^{-1}}$. For each angle $\theta$ the mean differential pressure between the static $P_\theta$ and a reference pressure was measured with a manometer (dynamic range 50 Pa), and the corresponding pressure coefficient was calculated according to:

$$C_P = (P_\theta - P_{\theta=0})/\tfrac{1}{2}\rho U_J^2. \tag{A 1}$$

Here, $P_{\theta=0}$ is the mean pressure at $\theta = 0^\circ$ and in figure 24, $C_P$ is plotted versus the yaw angle. In the range of $\pm 5^\circ$, we observe $-0.001 < C_P < 0$ and the variation among the different probes is small.

### A.2. *Mean static pressure calibration*

Mean static pressure probe calibrations were performed as follows. A standard Prandtl tube and a static probe were set parallel with each other in the potential core of a jet. A flexible rubber tube, 2 m in length, connects the outlets of the static pressure probe and the static tube of the Prandtl probe to a manometer (dynamic range is 50 Pa). The pressure difference $\Delta P$ is then measured for different jet velocities $U_J$ and probe dimensions. In figures 25(*a*) and 25(*b*) $\Delta P$ is plotted as absolute pressure difference and normalized with $\rho U_J^2$, respectively. For the probe bodies with an inner diameter of $\phi_2 = 1.0$ mm the smallest pinhole size ($\phi_1$) gives a negative $\Delta P$, while a minute positive $\Delta P$ is observed for the largest pinhole size. On the other hand, for the smallest probe (probe 2), the pressure difference gives a large positive value. It seems that $\Delta P$ is a function of both $\phi_1$ and $\phi_2$ in absolute values but fairly constant in terms of the dynamic pressure. Furthermore, the flexible rubber tube connecting the static tube with the manometer has some influence. It is clear that the situation is complex; however, the mean pressure measured by the five different probe sizes across the boundary layer at $R_\theta = 10\,500$ collapse well when a correction is made according to the calibration (cf. figure 26, where the pressure is the Gauge pressure).

The early analysis of Goldstein (1936) indicated that a static tube reads a pressure equal to $P_m = P + k\rho(v_{r.m.s.}^2 + w_{r.m.s.}^2)$, where $v_{r.m.s.}$ and $w_{r.m.s.}$ are the wall-normal and spanwise root-mean-square (r.m.s.) velocities, respectively, and $k$ is a small coefficient. The effect of turbulence on the measured value of static tubes seems to be much

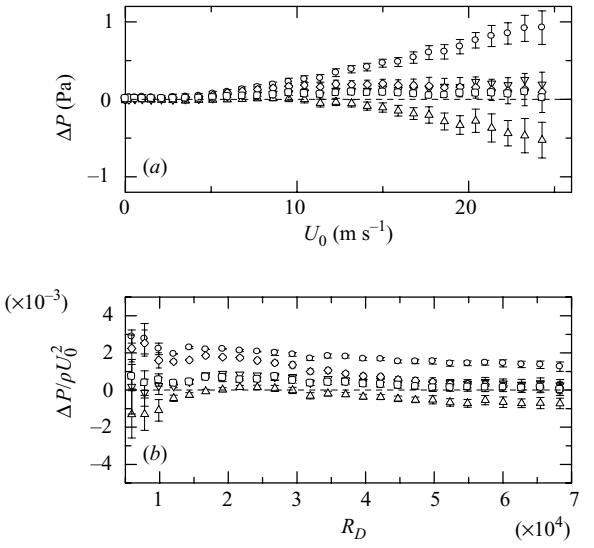


FIGURE 25. $\Delta P$ indicates pressure difference between the present pressure probes and the static pressure measured by a Prandtl tube in the centre of a jet. On the abscissa the jet-diameter ($D$) Reynolds number is shown. (*a*) Pressure difference in absolute value, (*b*) pressure difference normalized with twice the dynamic pressure. For symbols see table 2.

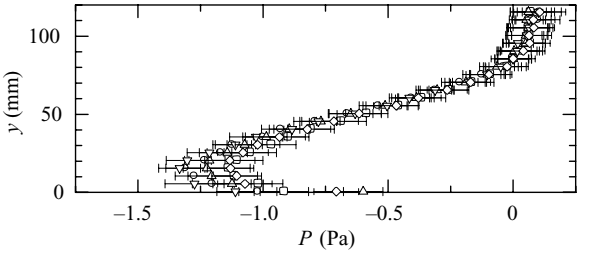


FIGURE 26. Static mean pressure distribution through the boundary layer measured with five different sized probes. For symbols see table 2.

smaller than previously known as long as the static tube and pinholes are made small enough (Chue 1975).

### A.3. *Dynamic signal treatment*

When measuring static pressure fluctuations there is not only a direct influence from the probe dimensions chosen, but also an indirect one from physical flow phenomena that appear inside the probe. Here, this is discussed and the calibration procedure is presented which accounts for all effects by numerical treatment of the static pressure signal.

The calibration of the static pressure probe, operated with the transducer or the microphone as pressure sensor, is done as follows. The probe is set parallel to an opened reference microphone in front of a loudspeaker. A fluctuating pressure stream is generated by a random noise generator and the two signals are acquired simultaneously. The output signal from the pressure probe $p_s(t)$ will not be the same as the signal $p_r(t)$ measured by the reference microphone, due to probe influence, Helmholtz resonance, and standing waves.

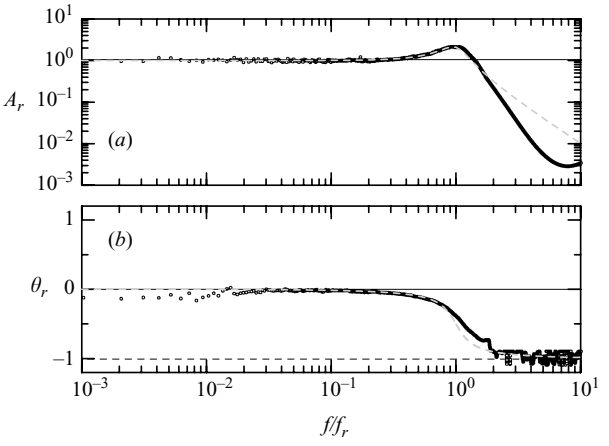


FIGURE 27. (*a*) Amplitude ratio and (*b*) phase delay (normalized with $\pi$) due to the HR as a function of frequency normalized by the HR frequency $f_r$. The symbols are obtained by calibration and the grey dashed line is obtained from the model given by equations (A 3) and (A 4).

The frequency response of the system is limited by the Helmholtz resonator (abbreviated as HR) caused by the tube and sensor cavity (cf. Kobashi 1957; Toyoda *et al.* 1993). This HR frequency is calculated as

$$f_r = \frac{U_s}{2\pi}\sqrt{\frac{S}{L_3 V}}, \tag{A 2}$$

where $V$ is the cavity volume, $L_3$ is the tube length, $U_s$ is the speed of sound and $S$ is the cross-sectional area (see also figure 1). For instance, with $V = \pi d^2 L_c/4$ and $S = \pi(\phi_2)^2/4$ the resonant frequency is 2.5 kHz and 11.1 kHz for the microphone ($d = 7.0$ mm, $\phi_2 = 1.0$ mm, $L_3 = 18.5$ mm) and the transducer ($d = 1.6$ mm, $\phi_2 = 1.0$ mm, $L_3 = 18.5$ mm), respectively. The amplitude ratio variation and phase delay between the two signals $p_s$ and $p_r$ can be computed by applying the simple HR model:

$$A_r = \left[\left\{1 - \left(\frac{f}{f_r}\right)^2\right\}^2 + \left(\frac{2\xi f}{f_r}\right)^2\right]^{-1/2}, \tag{A 3}$$

$$\theta_r = -\tan^{-1}\left\{\frac{2\xi\,(f/f_r)}{1-(f/f_r)^2}\right\}, \tag{A 4}$$

where $\xi$ is a numerical constant (JSME 1985). This model does not contain the effects of pinhole size, hole shape, and tube thickness. It should be noted that equations (A 3) and (A 4) give an approximation to the measured $A_r$ and $\theta_r$, obtained through fast-Fourier-transform (FFT) analysis, and are only reproduced here to show the potential of this HR model to capture the shape as a whole. In figure 27 a comparison between the model and the measured result is shown. Once the measured $A_r$ and $\theta_r$ have been calculated they are used to numerically remove the HR in Fourier space from all the measured $p_s$ signals. This calibration procedure is necessary in order to correct the data from the probe influence and the HR frequency, and in figure 28 an illustration of the result is shown. Although the original fluctuation $p_s$ differs significantly from $p_r$, once the effect of HR is removed, the signals match excellently.

A standing wave inside the pressure tube may also cause a small disturbance to the pressure fluctuations. The frequency of the standing wave is given by $f_s = U_s/\lambda_s$

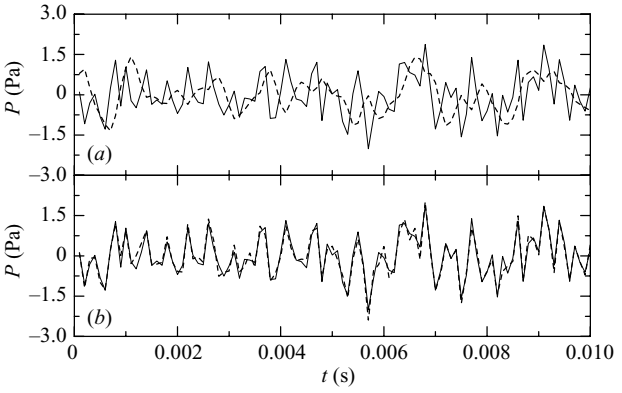


FIGURE 28. (*a*) The solid line is the reference microphone output and the dashed line is the measured static pressure signal. When the HR is removed numerically, the static pressure signal matches the reference probe signal as indicated in (*b*).

(where $\lambda_s/4 = L_3$), which gives a $f_s$ of about 7.1 kHz for probe 1. Another possible limitation may be the spatial resolution of the probe which may be limited by the pinhole size as well as the circumference of the probe itself. For instance, in the log region at $R_\theta = 12\,000$ the ratio between the pinhole diameter and the Kolmogorov scale can be estimated as $d/\eta = 1.9$ for probe 2.

### A.4. *Background noise*

A common problem in achieving accurate pressure measurements, in turbulent boundary layers, is the inherent signal contamination resulting from facility-induced noise. These acoustic disturbances are of low frequency, generally well below 100 Hz, and for low Reynolds numbers they dominate the pressure signal. On the other hand, for sufficiently high Reynolds numbers the noise contamination is often neglected since the turbulent fluctuations overwhelm the low-frequency disturbances.

Here, the static pressure $p_s(t)$ measured at $y = 120$ mm from the wall and the wall pressure fluctuation $p_w(t)$ are analysed in order to evaluate the background noise level. In this experiment, the boundary layer thickness is 65 mm at most, i.e. the probe position is about twice this thickness, implying that the two signals are totally uncorrelated. The pressures may be divided into two parts, the background noise due to acoustics and vibrations, denoted $p^b(t)$, and the true pressure fluctuation, denoted $p'(t)$, according to

$$p_s(t) = p'_s(t) + p^b_s(t), \quad p_w(t) = p'_w(t) + p^b_w(t). \tag{A 5}$$

The correlation function between the two signals is calculated as

$$\langle p_s p_w \rangle = \langle p'_s p'_w \rangle + \langle p^b_s p^b_w \rangle, \tag{A 6}$$

because both $p^b_s$ and $p^b_w$ are independent of the turbulent statistics. Furthermore, $\langle p'_s p'_w \rangle \simeq 0$ since the static pressure is measured at $y \simeq 2\delta$. This implies that the root mean square of the background noise is $p^b_{r.m.s.} \equiv \sqrt{\langle p^b_s p^b_w \rangle} \simeq \sqrt{\langle p_s p_w \rangle}|_{y \simeq 2\delta}$. In this experiment $p^b_{r.m.s.}$ decreases as a function of Reynolds number when normalized by outer variables ($p^b_{r.m.s.}/\rho U_0^2$) and asymptotes to a constant value of about $5 \times 10^{-4}$.

The frequency spectrum of $p_s$ is computed and shown in figure 29. It is noted that for frequencies below 100 Hz the data are contaminated by low-frequency noise. Furthermore, the sharp peak around 300 Hz is caused by acoustic noise from the

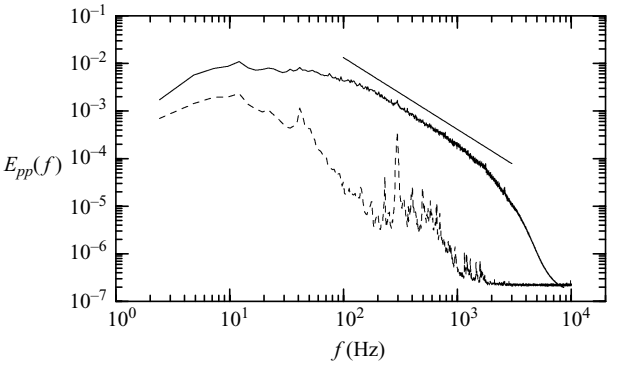


FIGURE 29. Static pressure spectrum measured at $y = 20$ mm (solid line) and in the free stream $y = 120$ mm (dashed line). Straight solid line represents the power-law relation defined by equation (2.8) with $\gamma_p = -1.5$.

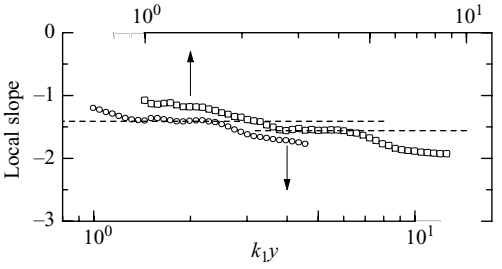


FIGURE 30. Local slope of the spectrum $\partial \log E_{pp}/\partial \log k_1$ computed at the position $y^+ = 160$ (open circles) and $y^+ = 340$ (open squares) in the overlap region at $R_\theta = 8920$. The exponent $\gamma_p$ is obtained by averaging the constant local slope region. $\gamma_p = -1.40 \pm 0.02$ for $y^+ = 160$ and $\gamma_p = -1.54 \pm 0.02$ for $y^+ = 340$, respectively, where error is evaluated by the standard deviation.

wind tunnel fan. In the high-frequency region, i.e. in the inertial range and in the dissipation range, acoustic noise effects are small. The correlation function with time lag $\tau$, $\langle p_s(t+\tau)p_w(t)\rangle$, has also been computed and by adopting the Taylor hypothesis $(U(y)\cdot\tau)$ the spatial correlation in the streamwise direction between the static and wall pressures is obtained. Here, $U(y)$ is the local mean velocity at $y$. The correlation coefficient $C_\tau \equiv \langle p_s(t+\tau)p_w(t)\rangle/(\sigma_s\sigma_w)$, where $\sigma_s = \sqrt{\langle p_s^2\rangle}$ and $\sigma_w = \sqrt{\langle p_w^2\rangle}$, decreases with the spatial distance and becomes close to zero for large separations, $\tau U(y) \geqslant 2.0$ m. Thus, the low-frequency noise is associated with motions of a few metres in spatial scale. Background noise cannot be removed instantaneously from the pressure signal without simultaneously measuring the pressure signal in the free stream, but may be corrected for in the statistical values, such as root mean square, skewness, and flatness. In the inner region of the boundary layer, $p^b_{r.m.s.}$ is much smaller than $p_s$ and $p_w$, implying that the correction would be very small; however it may be of influence in the outer region.

## Appendix B. Error analysis of spectral slope

Here, the errors contained in the spectral slope $\gamma_p$ are discussed. Figure 30 shows the local slope of the spectrum $\partial \log E_{pp}/\partial \log k_1$ computed at the positions $y^+ = 160,\ 340$

in the overlap region at $R_\theta = 8920$. The horizontal axis is the streamwise wavenumber normalized by the distance from the wall. The graph shows the plateau as indicated by the dashed line, which corresponds to the power-law region of the spectrum. The exponent $\gamma_p$ is obtained by calculating the average of this local slope. For instance, $\gamma_p = -1.40 \pm 0.02$ for $y^+ = 160$ and $\gamma_p = -1.54 \pm 0.02$ for $y^+ = 340$, where error is evaluated by the standard deviation. Thus, the error is small, which is in the order of $10^{-2}$.

As the distance $y$ increases, the power-law region is shifted towards higher frequencies, and the exponent $\gamma_p$ decreases systematically. These trends are observed in all data sets. Based on these observations, we can say that the power-law region is restricted to $1 < k_1 y$, but the exponent depends on the distance $y$ and the Reynolds number $R_\theta$. If error bars were plotted in figure 13, they would be smaller than the size of the symbols. Hence, we choose not to include error bars.

## REFERENCES


Abe, H., Matsuo, Y. & Kawamura, H. 2005 A DNS study of Reynolds-number dependence on pressure fluctuations in a turbulent channel flow. In *Proc. Fourth Intl Symp. on Turbulence and Shear Flow Phenomena, Williamsburg, VA USA, 27–29 June*, pp. 189–194.

Albertson, J. D., Katul, G. G., Parlange, M. B. & Eichinger, W. E. 1998 Spectral scaling of static pressure fluctuations in the atmospheric surface layer: The interaction between large and small scales. *Phys. Fluids* **10**, 1725–1732.

Alfredsson, P. H. & Johansson, A. V. 1984 Time scale in turbulent channel flow. *Phys. Fluids* **27**, 1974–1980.

Alfredsson, P. H., Johansson, A. V. & Kim, J. 1988 Turbulence production near walls: the role of flow structures with spanwise asymmetry. Studying Turbulence Using Numerical Simulation Databases – II. *Proc. 1988 Summer program, Center for Turbulence Research, Report* CTR-S88.

Alvelius, K. & Johansson, A. V. 2000 Les computations and comparison with kolmogorov theory for two-point pressure-velocity correlations and structure functions for globally anisotropic turbulence. *J. Fluid Mech.* **403**, 22–36.

Arad, I., Dhruva, B., Kurien, S., L'vov, V. S., Procaccia, I. & Sreenivasan, K. R. 1998 Extraction of anisotropic contribution in turbulent flows. *Phys. Rev. Lett.* **81**, 5330–5333.

Batchelor, G. K. 1951 Pressure fluctuations in isotropic turbulence. *Proc. Camb. Phil. Soc.* **47**, 359–374.

Bradshaw, P. 1967*a* Inactive motion and pressure fluctuation in turbulent boundary layers. *J. Fluid Mech.* **30**, 241–258.

Bradshaw, P. 1967*b* The turbulence structure of equilibrium boundary layers. *J. Fluid Mech.* **29**, 625–645.

Bull, M. K. 1996 Wall-pressure fluctuations beneath turbulent boundary layers: Some reflections on forty years of research. *J. Sound Vib.* **190**, 299–315.

Cadot, O., Douady, S. & Couder, Y. 1995 Characterization of the low-pressure filaments in a three-dimensional turbulent shear flow. *Phys. Fluids* **7**, 630–646.

Cao, N., Chen, S. & Doolen, G. D. 1999 Statistics and structures of pressure in isotropic turbulence. *Phys. Fluids* **11**, 2235–2250.

Chue, S. H. 1975 Pressure probes for fluid measurement. *Prog. Aerospace Sci.* **16**, 147–223.

Corcos, G. M. 1963 Resolution of pressure in turbulence. *J. Acoustic. Soc. Am.* **35**, 192–199.

Eckelmann, H. 1989 A review of knowledge of pressure fluctuations. In *Proc. 1988 Zoran Zaric Memorial Conference, Dubrovnik, Croatia* (ed. S. J. Kline & N. H. Afgan), pp. 328–347.

Eggels, J. G. M., Unger, F., Weiss, M. H., Westerweel, J., Adrian, R. J., Friedrich, R. & Nieuwstadt, F. T. M. 1994 Fully developed turbulent pipe flow: a comparison between direct numerical simulation and experiment. *J. Fluid Mech.* **268**, 175–209.

Elliot, J. A. 1972 Microscale pressure fluctuations measured within the lower atmospheric boundary layer. *J. Fluid Mech.* **53**, 351–383.

Farabee, T. M. & Casarella, M. J. 1986 Measurements of fluctuating wall pressure for separated reattached boundary-layer flows. *Trans. ASME: J. Vib. Acoust.* **108**, 301–307.

Farabee, T. M. & Casarella, M. J. 1991 Spectral features of wall pressure fluctuations beneath turbulent boundary layers. *Phys. Fluids* **3**, 2410–2420.

Fernholz, H. F. & Finley, P. J. 1996 The incompressible zero-pressure-gradient turbulent boundary layer: An assessment of the data. *Prog. Aerospace Sci.* **32**, 245–311.

Gedney, C. J. & Leehey, P. 1991 Wall pressure fluctuations during transition on a flat plate. *Trans. ASME: J. Vib. Acoust*. **113**, 255–266.

George, W. K., Beuther, P. D. & Arndt, R. E. A. 1984 Pressure spectra in turbulent free shear flows. *J. Fluid Mech.* **148**, 155–191.

Goldstein, S. A. 1936 A note on measurement of total head and static pressure in a turbulent stream. *Proc. R. Soc. Lond.* A **155**, 570–575.

Gotoh, T. & Fukayama, D. 2001 Pressure spectrum in homogeneous turbulence. *Phys. Rev. Lett.* **86**, 3775–3778.

Gotoh, T. & Rogallo, R. S. 1999 Intermittency and scaling of pressure at small scales in forced isotropic turbulence. *J. Fluid Mech.* **396**, 257–285.

Gravante, S. P., Naguib, A. M., Wark, C. E. & Nagib, H. M. 1998 Characterization of the pressure fluctuations under a fully developed turbulent boundary layer. *AIAA J.* **36**, 1808–1816.

Heisenberg, W. 1948 Zür Statistischen Theorie der Turbulenz. *Z. Phys.* **124**, 628–657.

Hill, R. J. 2002 Scaling of acceleration in locally isotropic turbulence. *J. Fluid Mech.* **452**, 361–370.

Hill, R. J. & Wilczak, J. M. 1995 Pressure stucture functions and spectra for locally isotropic turbulence. *J. Fluid Mech.* **296**, 247–269.

Hinze, J. O. 1975 *Turbulence*. McGraw-Hill.

Iida, A., Otaguro, T., Kato, C. & Shimode, S. 1998 Analysis of aerodynamic sound source with measurement of static-pressure fluctuation. *JSME* **64**, 2057–2064 (in Japanese).

Inoue, E. 1951 The application of the turbulence theory to the large-scale atmospheric phenomena. *Geophys. Mag.* **23**, 1–14.

Ishihara, T., Kaneda, Y., Yokokawa, M., Itakura, K. & Uno, A. 2003 Spectra of energy dissipation, enstropy and pressure by high-resolution direct numerical simulations of turbulence in a periodic box. *J. Phys. Soc. Japan* **72**, 983–986.

Jeong, J., Hussain, F., Schoppa, W. & Kim, J. 1997 Coherent structures near the wall in a turbulent channel flow. *J. Fluid Mech.* **332**, 185–214.

Johansson, A. V., Alfredsson, P. H. & Kim, J. 1991 Evolution and dynamics of shear-layer structures in near-wall turbulence. *J. Fluid Mech.* **224**, 579–599.

Jones, B. G., Adrian, R. J., Nithiandan, C. K. & Planchon, H. P. 1979 Spectra of turbulent static pressure fluctuation in jet mixing layers. *AIAA J.* **17**, 449–457.

JSME 1985 *JSME Data Book : Flow Measurement*. The Japan Society of Mechanical Engineering.

Keith, W. L., Hurdis, D. A. & Abraham, B. M. 1992 A comparison of turbulent boundary layer wall-pressure spectra. *Trans. ASME*: *J. Fluids Engng* **114**, 338–347.

Kida, S. & Miura, H. 1998 Identification and analysis of vortical structures? *Eur. J. Mech.* B-*Fluids* **17**, 471–488.

Kim, J. 1989 On the structure of pressure fluctuations in simulated turbulent channel flow. *J. Fluid Mech.* **205**, 421–451.

Klewicki, J. C., Perkins, B. F. & Metzge, M. M. 2005 Wall pressure statistics in a high reynolds number turbulent boundary layer. In *Proc. Fourth Intl Symp. on Turbulence and Shear Flow Phenomena, Williamsburg, VA USA, 27–29 June* (ed. J. A. C. Humphrey, T. B. Gatski, J. K. Eaton, R. Friedrich, N. Kasagi & M. A. Leschziner), pp. 21–26.

Kobashi, Y. 1957 Measurements of pressure fluctuation in the wake of cylinder. *J. Phys. Soc. Japan* **12**, 533–543.

Kobashi, Y. & Ichijo, M. 1986 Wall pressure and its relation to turbulent structure of a boundary layer. *Exps. Fluids* **4**, 49–55.

Kobashi, Y., Komoda, H. & Ichijo, M. 1984 Wall pressure fluctuation and the turbulence structure of a boundary layer. In *Turbulence and Chaotic Phenomena in Fluids* (ed. T. Tatsumi), pp. 461–466. Elsevier.

Kobashi, Y., Kono, N. & Nishi, T. 1960 Improvement of a pressure pickup for the measurements of turbulence characteristics. *J. Aero/Space Sci.* **27**, 149–151.

Kurien, S., L'vov, V. S., Procaccia, I. & Sreenivasan, K. R. 2000 Scaling structure of the velocity statistics in atmospheric boundary layers. *Phys. Rev.* E **61**, 407–421.

La Porta, A., Voth, G. A., Crawford, A. M., Alexander, J. & Bodenschatz, E. 2001 Fluid particle accelerations in fully developed turbulence. *Nature* **409**, 1017–1019.

Lindgren, B. 2002 Flow facility design and experimental studies of wall-bounded turbulent shear-flow. PhD thesis, TRITA-MEK Tech. Rep. 2002:16, Dept. Mech., KTH, Stockholm, Sweden.

Lindgren, B., Johansson, A. V. & Tsuji, Y. 2004 Universality of probability density distributions in the overlap region in high reynolds number turbulent boundary layer. *Phys. Fluids* **16**, 2587–2591.

Löfdahl, L. & Gad-el-Hak, M. 1999 MEMS-based pressure and shear stress sensors for turbulent flow. *Meas. Sci. Technol.* **10**, 665–686.

Lueptow, R. M. 1995 Transducer resolution and the turbulent wall pressure spectrum. *J. Acoust. Soc. Am.* **97**, 370–378.

Monin, M. S. & Yaglom, A. M. 1971 *Statistical Fluid Mechanics, Vol. 2*. The MIT Press.

Moser, R. D., Kim, J. & Mansour, N. N. 1999 Direct numerical simulation of turbulent channel flow up to $Re_\tau = 590$. *Phys. Fluids* **11**, 943–945.

Naka, Y., Omori, T., Obi, S. & Masuda, S. 2005 Experimental study on velocity-pressure correlation in turbulent mixing layer out of equilibrium state. In *Proc. Fourth Intl Symp. on Turbulence and Shear Flow Phenomena, Williamsburg, VA USA, 27–29 June* (ed. J. A. C. Humphrey, T. B. Gatski, J. K. Eaton, R. Friedrich, N. Kasagi & M. A. Leschziner), pp. 1125–1130.

Nepomuceno, H. G. & Lueptow, R. M. 1997 Pressure and shear stress measurements at the wall in a turbulent boundary layer on a cylinder. *Phys. Fluids* **9**, 2732–2739.

Obukhov, A. M. 1949 Pressure fluctuations in a turbulent flow. *Dokl. Akad. Nauk SSSR* **66**, 17–20.

Obukhov, A. M. & Yaglom, A. M. 1951 The microstructure of turbulent flow. *NACA TM* 1350.

Österlund, J. M. 1999 Experimental studies of zero pressure-gradient turbulent boundary layer flow. PhD thesis, TRITA-MEK Tech. Rep. 1999:16, Dept. Mech., KTH, Stockholm, Sweden.

Österlund, J. M., Johansson, A. V., Nagib, H. M. & Hites, M. H. 2000 A note on the overlap region in turbulent boundary layers. *Phys. Fluids* **12**, 1–4.

Panton, R. L., Goldman, A. L., Lowery, R. L. & Reischman, M. M. 1980 Low-frequency pressure fluctuations in axisymmetric turbulent boundary layers. *J. Fluid Mech.* **97**, 299–319.

Panton, R. L. & Linebarger, J. H. 1974 Wall pressure spectra calculations for equilibrium boundary layers. *J. Fluid Mech.* **65**, 261–287.

Perry, A. E., Henbest, S. M. & Chong, M. S. 1986 A theoretical and experimental study of wall turbulence. *J. Fluid Mech.* **165**, 163–199.

Pumir, A. 1994 A numerical study of pressure fluctuations in three-dimensional, incompressible, homogeneous, isotropic turbulence. *Phys Fluids* **6**, 2071–2083.

Schewe, G. 1983 On the structure and resolution of wall-pressure fluctuations associated with turbulent boundary-layer flow. *J. Fluid Mech.* **134**, 311–328.

Shaw, R. 1960 The influence of hole dimensions on static pressure measurements. *J. Fluid Mech.* **9**, 550–556.

Shen, X. & Warhaft, Z. 2000 The anisotropy of the small scale structure in high reynolds number turbulent shear flow. *Phys. Fluids* **12**, 2976–2989.

Skote, M. 2001 Studies of turbulent boundary layer flow through direct numerical simulation. PhD thesis, TRITA-MEK Tech. Rep. 2001:01, Dept. Mech., KTH, Stockholm, Sweden.

Spalart, P. R. 1988 Direct simulation of a turbulent boundary layer up to $R_\theta = 1410$. *J. Fluid Mech.* **187**, 61–98.

Sreenivasan, K. R. & Antonia, R. A. 1997 The phenomenology of small-scale turbulence. *Annu. Rev. Fluid Mech.* **29**, 435–472.

Tanifuji, N., Ichijo, M., Iida, S. & Kobashi, Y. 1986 Coherent structures in fully developed turbulent pipe flow. *Bull. JSME* **29**, 1156–1162.

Townsend, A. A. 1976 *The Structure of Turbulent Shear Flow,* 2nd edn. Cambridge University Press.

Toyoda, K., Okamoto, T. & Shirahama, Y. 1993 Eduction of vortical structures by pressure measurements in noncircular jet. *Fluid Mech. Applics.* **21**, 125–136.

Tsuji, Y. 2003 Large-scale anisotropy effect on small-scale statistics over rough wall turbulent boundary layers. *Phys. Fluids* **12**, 3816–3828.

Tsuji, Y., Fransson, J. H. M., Alfredsson, P. H. & Johansson, A. V. 2005*a* Pressure statistics in high-Reynolds number turbulent boundary layer. In *Proc. Fourth Intl Symp. on Turbulence*

*and Shear Flow Phenomena, Williamsburg, VA USA, 27–29 June* (ed. J. A. C. Humphrey, T. B. Gatski, J. K. Eaton, R. Friedrich, N. Kasagi & M. A. Leschziner), pp. 27–32.

Tsuji, Y. & Ishihara, T. 2003 Similarity scaling of pressure fluctuation in turbulence. *Phys. Rev.* E **68**, 026309.

Tsuji, Y. & Ishihara, T. 2006 Pressure statistics in turbulence. In *IUTAM Symposium on Elementary Vortices and Coherent Structures: Significance in Turbulence Dynamics, Kyoto Japan, 26–28 October, 2004*, pp. 163–170. Springer.

Tsuji, Y., Lindgren, B. & Johansson, A. V. 2005*b* Self-similar profile of probability density functions in zero-pressure gradient turbulent boundary layers. *Fluid Dyn. Res.* **37**, 293–316.

Vedula, P. & Yeung, P. K. 1999 Similarity scaling of acceleration and pressure statistics in numerical simulation of isotropic turbulence. *Phys . Fluids* **11**, 1208–1220.

Voth, G. A., Satyanarayan, K. & Bodenschatz, E. 1998 Lagrangian acceleration measurements at large Reynolds numbers. *Phys. Fluids* **10**, 2268–2280.

Willmarth, W. W. 1975 Pressure fluctuations beneath turbulent boundary layers. *Annu. Rev. Fluid Mech.* **7**, 13–38.

Yaglom, A. M. 1949 Acceleration field in a turbulent flow. *Dokl. Akad. Nauk SSSR* **67**, 795–798.